

The Accuracy of Airborne Interferometric SAR'S

Ernesto Rodríguez, David A. line], and Søren N. Madsen
Jet Propulsion laboratory
California Institute of Technology
4800 Oak Grove Dr., Pasadena, CA 91109

(Submitted to IEEE Trans. AES)

Abstract: We extend the analysis of the accuracy of Interferometric SAR (InSAR) for topographic mapping to cover a variety of topics which have not been previously examined in the literature. These include deriving the position measurement sensitivities for arbitrary interferometer geometries, scatterer distributions, point target responses, and for InSARs using frequency diversity (following the proposal of Gatelli et al. [1]). The relative merit of single frequency and two-frequency InSAR systems is discussed, and the superiority of the latter is shown quantitatively. The effect of tropospheric propagation is also considered and it is shown how this may be incorporated easily into the standard InSAR processing.

1. Introduction

Interferometric SAR (InSAR) is one of the most promising techniques for obtaining very high resolution and accuracy topographic data from space and airborne instruments. Unlike more mature methods, such as stereo photography, the technique is still in its development stage. One of the current advantages of stereo photography data is that its limitations are well understood and formal map errors can be derived. To advance InSAR topographic mapping to the same level, it is important to understand its inherent capabilities and limitations. The first systematic investigation of InSAR errors was performed by Li and Goldstein [2]. Subsequently, Rodriguez and Martin [3] presented a refined analysis which included the effect of volume scattering.

The purpose of this paper is to present a systematic analysis of the InSAR error budget for airborne systems including various effects previously ignored. In the first and second sections, we derive the interferometer positioning equations and their sensitivities for an arbitrary imaging geometry: "squinted" SAR processing and arbitrary interferometer baseline orientations are allowed. Most of the error sources identified in these sections have a simple geometric interpretation and are not intrinsically related to the scattering characteristics of the imaged scene. This is not the case for the interferometric phase, and we devote the next three sections to examining this error source in detail. We extend the previous analyses to include the possibility of using a two-frequency interferometric system, following an idea introduced by Gatelli et al. [1], and contrast the performance of this method against more traditional single frequency interferometers. Finally, we examine the effects of the troposphere on InSAR performance and show how the interferometric equations may be changed simply to account for signal delay and ray bending.

2. The Interferometric Equations

An InSAR system determines the position vector of a pixel given the following measurements: 1) \vec{r}_g , the position vector of a point, which we take to be half way between the two interferometer antennas (see figure 1); 2) \hat{r}_+ and \hat{r}_- , the electromagnetic paths lengths to a resolution cell (including ray bending) from the two interferometric antennas;

3) Φ , the interferometric phase difference; 4) \vec{B} , the interferometric baseline (the convention used is that $\vec{r}_+ = \vec{B} + \vec{r}_-$); and, 5) \vec{v} , the platform velocity. It is convenient to define $\vec{r} = (\vec{r}_+ + \vec{r}_-)/2$ as the vector from the reference position to the resolution cell, and \hat{n} as a unit vector pointing from the reference point to the resolution cell (see figure 1).

These measurements, together with the following auxiliary equations

$$\Phi = -k(\vec{r}_+ - \vec{r}_-) \quad (1)$$

$$2\pi f_D = -2k \frac{d\vec{r}}{dt} = 2k \frac{d\vec{r}}{dr} \hat{n} \cdot \vec{v} \quad (2)$$

$$\hat{n} \cdot \hat{n} = 1 \quad (3)$$

must be used to determine the line of sight direction to the pixel, \hat{n} , and the geometric range, r . In the previous equations, k is the wavenumber, and f_D is the Doppler frequency. Given \hat{n} and r , the position vector to the resolution cell, \vec{r}_g , can be obtained by means of the equation

$$\vec{r}_g = \vec{r}_g + r\hat{n} \quad (4)$$

For most airborne applications, terms of order $(B/r)^3$ and ray bending may be ignored when considering the interferometer sensitivity. In this case, the first two interferometric equations may be written as

$$\hat{n} \cdot \vec{B} = \frac{-\Phi}{k} \equiv \hat{\Phi} \quad (5)$$

$$\hat{n} \cdot \vec{v} = \frac{\pi f_D}{k} \equiv \hat{f} \quad (6)$$

An interferometer location algorithm based on these equations was first presented by Madson *et al.* [4]. Below, we shall show that the effects of tropospheric propagation do not significantly change the form of these equations. We will use the simplified equations in our subsequent analysis since the use of the exact equations adds unnecessarily to the algebra without contributing to physical understanding, or, in any significant way, to the numerical accuracy of the error analysis.

The interferometric positioning equations can be given a geometric interpretation: equations (5) and (6) define two cones with axes in the \vec{B} and \vec{v} directions, respectively. A point in three dimensional space is defined as the locus of intersection of the two cones and the sphere of radius r . This locus is not uniquely defined: in general, the cones intersect along two straight lines starting at the origin, symmetric about the plane spanned by \vec{B} and \vec{v} . The intersection with the range sphere occurs at two points. Discrimination between these two points is accomplished by specifying which side of the \vec{B} - \vec{v} plane the point occupies. Mathematically, this is reflected by the fact that equations (5) and (6) determine two components of \hat{n} : the ones in the plane determined by the baseline and velocity vectors. The third component is specified (up to a sign) by requiring the look direction be a unit vector.

3. Interferometric Sensitivity Equations for Arbitrary Geometry

From equation (4), the error in the interferometric measurement can be written as

$$\delta \vec{r}_g = \delta \vec{r}_g + \hat{n} \delta r + r \delta \hat{n} \quad (7)$$

The first two error sources are simple to characterize. The first one corresponds to a shift in the coordinate system; the second to a timing error.

It is clear that any errors in the baseline or velocity which do not affect equations (5) and (6) will not introduce positioning errors: i.e., the interferometer is insensitive to errors which are perpendicular to \hat{n} . This implies that for a sidelooking system, speed errors will not introduce positioning errors. Similarly, if the antenna baseline is orthogonal to the look direction, a dilation of the baseline will not introduce positioning errors (to the accuracy of the previous equations). This is of great practical advantage since it implies that one need only concern oneself with the component of the error along the look direction when designing a baseline or velocity monitoring system. In addition, it greatly simplifies the form of the sensitivity equations.

Characterization of the last error source can be made by noting that, since \hat{n} is a unit vector

$$\delta \hat{n} \cdot \hat{n} = 0 \quad (8)$$

Hence, errors due to this term must lie in a plane perpendicular to the look direction. The error can be further characterized by specifying the error source: phase error, velocity error, or baseline error. The measurement of interferometric phase and platform velocities are independent. Differentiating equations (5) and (6) one obtains, respectively

$$\frac{\partial \hat{n}}{\partial \vec{v}} \cdot \vec{B} = 0 \quad (9)$$

$$\frac{\partial \hat{n}}{\partial \vec{B}} \cdot \vec{v} = 0 \quad (10)$$

Together with equation (8), the first equation implies that an error due to velocity errors must be simultaneously perpendicular to the look and the baseline directions. This condition is only satisfied if the position error lies along the axis defined by the vector $\hat{n} \times \vec{B}$. Similarly, an error in the baseline will induce a position error which lies on the axis defined by the vector $\hat{n} \times \vec{v}$. A simple consequence of these results is that if the look direction, the baseline, and the z axis are coplanar, an error in velocity will not produce an error in height (but will still produce an error in location).

The characterization of position errors due to phase errors is aided by the following relation, which is obtained by taking the total derivative of equation (6), and noting that the Doppler frequency is set arbitrarily

$$\delta \hat{n} \cdot \vec{v} + \hat{n} \cdot \delta \vec{v} = 0 \quad (11)$$

i.e., there will be no error along the velocity direction unless there is a velocity error. Thus, a phase error must induce position errors which are simultaneously perpendicular to \hat{n} and \vec{v} . This implies that the induced position errors must lie on the axis defined by the vector $\hat{n} \times \vec{v}$; i.e., on the same axis as baseline errors.

The geometric characteristics of errors in \hat{n} due to errors in the wavenumber, k , or, equivalently, in the speed of light or wavelength, are not as apparent from the previous equations as those for velocity and baseline errors. Nevertheless, it can be argued that this error must satisfy two requirements: first, as with the other errors, it must be perpendicular to the look direction; second, if the look direction is perpendicular to the baseline, the phase difference is zero, independent of the wavenumber. Therefore, this error will be minimized as the look direction approaches the direction normal to the baseline, when the phase error is least sensitive to the wavenumber chosen.

Appendix A presents a detailed derivation of the sensitivity equations which include the effects outlined above. The final result is given by the vector equation

$$\delta \vec{r}_g = \delta \vec{r}_a + \hat{n} \delta r + r \frac{\hat{n} \times \hat{v}}{\hat{b} \cdot (\hat{n} \times \hat{v})} \left[\frac{\delta \tilde{\Phi}}{B} - \hat{n} \cdot \frac{\delta \vec{B}}{B} \right] + r \frac{\hat{n} \times \hat{b}}{\hat{b} \cdot (\hat{n} \times \hat{v})} \hat{n} \cdot \frac{\delta \vec{v}}{v} + r \left[\frac{\hat{v} \times \hat{b}}{\hat{b} \cdot (\hat{n} \times \hat{v})} - \hat{n} \right] \frac{\delta k}{k} \quad (12)$$

where $\hat{b} = \vec{B}/B$ is the unit vector along the baseline direction. This form clearly shows that an error, $\delta \vec{B}$, in the baseline is completely equivalent to an error in the phase given by $\delta \Phi = k \hat{n} \cdot \delta \vec{B}$. It also shows that when the look direction is along the direction $\hat{v} \times \hat{b}$, the position error is independent of wavenumber, as was argued previously.

The determination of positioning, velocity, and baseline errors is conceptually straightforward, although often difficult in practice. Up to a factor, which is roughly of unit magnitude, the previous equations show that the fractional position error, $|\delta \vec{r}_g/r|$, is of the same order as $|\hat{n} \cdot \frac{\delta \vec{v}}{v}|$, $|\hat{n} \cdot \frac{\delta \vec{B}}{B}|$, or $\delta \vec{r}_a/r$. For geologic airborne applications, a typical requirement is $|\delta \vec{r}_g/r| \sim 10^{-4}$. For spaceborne applications, this requirement is even more stringent: $|\delta \vec{r}_g/r| \sim 10^{-6}$. It is clear that these requirements place great demands on the navigation and baseline determination sensors,

4. Interferometric Phase Noise

Unlike the geometric terms, which are inherent to all triangulation schemes, the phase error is intrinsic to the InSAR technique and we devote the next three sections to studying it in detail. The phase error can be divided into systematic and random components. Systematic errors can be caused by systematic changes in the electrical path traversed by the interferometric signal, or by effects intrinsic in the observed scene, such as non-homogeneous scenery or penetration in a vegetation canopy. The former type of error is straightforward to understand and model. Typical sources are radome inhomogeneities or multi-path effects. We deal with the latter source of error below.

Due to speckle and thermal noise in the return signal, the interferometric phase contains random errors. In Appendix B we show that, for homogeneous targets, the maximum likelihood estimator (MLE) of interferometric phase is given by

$$\hat{\Phi} = \arctan \left[\frac{\text{Im} \left(\sum_{k=1}^{N_L} v_+^{(k)} v_-^{*(k)} \right)}{\text{Re} \left(\sum_{k=1}^{N_L} v_+^{(k)} v_-^{*(k)} \right)} \right] \quad (13)$$

where N_L is the number of looks to be averaged.

Appendix B shows that the Cramer-Rao bound for the phase standard deviation is given by

$$\langle (\hat{\Phi} - \langle \hat{\Phi} \rangle)^2 \rangle' / ' = \frac{1}{\sqrt{2N_L}} \frac{\sqrt{1 - \gamma^2}}{\gamma} \quad (14)$$

where γ is the correlation between the signals in the two interferometric channels. The most important characteristic of this equation is that the phase noise is only a function of the number of looks and the correlation between the two interferometer channels, which will be derived below.

The MLE estimator is unbiased, and the phase variance can easily be obtained numerically, as shown by Li and Goldstein [2]. Figure 2 presents a comparison of the actual phase standard deviation against the Cramer-Rao bound for various values of the correlation. As can be seen, the phase standard deviation decreases much faster than $N_L^{-1/2}$ for the first four looks. The fact that this happens more quickly for two looks when the correlation is low is due to 27r ambiguity in the phase. As the number of looks increases, the higher correlated cases approach the asymptotic behavior more quickly. After four looks, the phase standard deviation is well approximated by the Cramer-Rao bound.

5. Interferometric Return Signal Characteristics from Distributed Targets

We consider an interferometer system with geometry as depicted in figure 1. We assume one transmitter and for each of the interferometer receivers, we model the interferometer coherent signal, v_i ($i = +, -$), for range r_0 and cross range coordinate x_0 , by

$$\begin{aligned} v_+(r_0 + A/2, x_0) &= A \int dz \int dS e^{-2ik_+ r_+} f(x, y, z) W_+(r_0 + A/2 - r_+, x_0 - x) + n_+ \\ v_-(r_0 - A/2 + \delta_r, x_0 + \delta_x) &= \int d\delta \int dz \int dS e^{-ik_-(r_+ + r_-)} f(x, y, z) \\ &\quad W_-((r_0 - A/2 - \delta_r) - r_-, (x_0 + \delta_x) - x) + n_- \end{aligned} \quad (15)$$

where n_i is the thermal noise contribution to the signals, dS is the infinitesimal area element on the plane perpendicular to z , k_i is the wavenumber ($= 2\pi/\lambda_i$) for the carrier frequency at each receiver, $W_i(r, x)$ is the system's range cross-range point target response, r_i represents the range from the i^{th} antenna to the scattering point, and A is a constant which depends

on the system parameters. We have assumed that both signals are offset by a deterministic range $\pm\Delta/2$ so that they will be coregistered in range. We have allowed for the existence of range and azimuth coregistration errors, δ_r and δ_x , respectively. We have also allowed the possibility for different carrier frequencies at each receiver. This can be achieved either by utilizing different parts of the transmitted bandwidth, or by transmitting and receiving from each antenna at different frequencies (in which case the term $r_+ + r_-$ becomes $2r_-$). Finally, we have assumed that the scattering characteristics do not change across the transmitted bandwidth.

Very often, single scattering (one bounce) is the dominant scattering mechanism from natural targets. We postpone the detailed treatment of multiple scattering for specific media and treat single scattering only in this paper. However, the effect of multiple scattering can be understood qualitatively. When only one transmitter is used, it is not difficult to convince oneself that, for a simple multiple bounce scattering mechanism where the path length is identical for both signals until the final scatterer, the interferometric phase measured is the same as that due to the final scatterer alone. Therefore the InSAR will estimate the look direction from this scattering event as being the direction to the last scatterer. However, due to the additional distance travelled by the rays, the return will be placed at a greater range than the return from the last scatterer. The magnitude of this range error depends on the length of the scattering path, which is a strong function of the scattering medium. Due to the reciprocity of the electromagnetic field (which only applies approximately to the second receiver), for any simple multiple bounce path that contributes to the interferometric phase there will also be a contribution from the time reversed path. This will cause the final interferometric phase to be an average of the interferometric phases due to scatterers at the ends of the scattering chain, thus setting the angular elevation equal to one corresponding to a point between these two points. When two transmitters are used, there is an additional phase contribution which acts as a noise term and is not as easy to interpret.

These considerations motivate us to assume that the surface scattering amplitude, $f(x, y, z)$, obeys the following equation

$$\langle f(x, y, z) f^*(x', y', z') \rangle = \sigma_0(x, y, z, \theta) \delta(x - x') \delta(y - y') \delta(z - z') \quad (16)$$

where $\sigma_0(x, y, z, \theta)$ is the normalized backscatter cross section per unit height for incidence angle θ . Notice that the more common normalized radar cross section is defined as

$$\sigma_0(x, y, \theta) = \int dz \sigma_0(x, y, z, \theta) \quad (17)$$

If the SAR coherent return signal has circular Gaussian statistics, as is often observed, a complete characterization of the interferometric return can be obtained by calculating the complex covariance matrix for v_+ and v_- . Using equation (16), and the fact n_1 and n_2

are uncorrelated, the complex covariance of v_+ and v_- is given by

$$\langle v_+(r_0 + \Delta/2, x_0) v_-^*(r_0 - \Delta/2 + \delta_r, x_0 + \delta_x) \rangle = |A|^2 \int dz \int dS \sigma_0(x, y, z, \theta) \exp[-ik_-(r_+ - r_-)] \exp(-i2\delta k r_+) W_+(r_0 + \Delta/2 - r_+, x_0 - x) W_-^*(r_0 - \Delta/2 + \delta_r - r_+, x_0 + \delta_x - x) \quad (18)$$

where we have defined the wavenumber difference as $\delta k = k_+ - k_-$.

To make further progress, we expand about r_0 and approximate

$$r_+ - r_- \approx \Delta + \vec{B} \cdot (1 - \hat{n}\hat{n}) \cdot \frac{\delta \vec{r}_0}{r_0} \equiv \Delta + \frac{\vec{B}_p}{r_0} \cdot \delta \vec{r}_0 \quad (19)$$

$$\Delta = |\vec{r}_0 + \frac{\vec{B}}{2}| - |\vec{r}_0 - \frac{\vec{B}}{2}| \quad (20)$$

where B_p is the projection of the interferometric baseline onto the direction perpendicular to the look direction, and $\vec{r} = \vec{r}_0 + \delta \vec{r}_0$. Equation (19) makes it apparent that locally there is a phase difference between two points only if their separation vector is nonzero in the $\vec{B}/|\vec{B}|$ direction. We decompose the scatterer height locally into a tilted plane component and an additional component, Z , representing the height above the mean tilted plane

$$z = x \tan \tau_x + y \tan \tau_y + Z \quad (21)$$

where the coordinates x, y , and z are measured from the expansion point, and τ_x and τ_y represent the surface slopes in the x and y directions, respectively, and we assume that the scatterer properties are only governed by their height above the mean tilted plane

$$\sigma_0(x, y, z, \theta_0) = \sigma_0(Z, \theta_0) \quad (22)$$

We expect this assumption to be good for most natural targets which have no sharply defined changes in surface brightness. This assumption is not as good for some inhabited areas, where sudden changes in the reflectivity are common, and we consider another model below to study these cases.

After some algebra, equation (18) can be integrated analytically to obtain the complex covariance. It is given by

$$\langle v_+ v_-^* \rangle = |A|^2 \frac{\cos \tau_y}{|\sin(\theta_0 - \tau_y)|} \exp[-i(k_+ \Delta + 2\delta k r_0)] \tilde{\sigma}(\kappa_z) \Gamma(\kappa_r + 2\delta k, \kappa_z \tan \tau_x, \delta_r, \delta_x) \quad (23)$$

$$\tilde{\sigma}(\kappa_z) = \int dZ \exp[-i\kappa_z Z] \sigma(Z) \quad (24)$$

$$\kappa_r = \frac{k_+ B_p}{r_0 \tan(\theta_0 - \tau_y)} \quad (25)$$

$$\kappa_z = \frac{k_+ B_p \cos \tau_y}{r_0 \sin(\theta_0 - \tau_y)} = \kappa_r \frac{\cos \tau_y}{\cos(\theta_0 - \tau_y)} \quad (26)$$

and the function $\Gamma(\kappa_r + 2\delta k, \kappa_z \tan \tau_x, \delta_r, \delta_x)$ is defined as

$$\begin{aligned}\Gamma(\kappa_r + 2\delta k, \kappa_z \tan \tau_x, \delta_r, \delta_x) &= \left(\frac{1}{2\pi}\right)^2 \int d\kappa_1 d\kappa_2 \exp[-i\delta_r(\kappa_1 + \kappa_r + 2\delta k)] \exp[-i\delta_x(\kappa_2 + \tan \tau_x \kappa_z)] \\ &\quad \tilde{W}_+(\kappa_1, \kappa_2) \tilde{W}_-(\kappa_1 + (\kappa_r + 2\delta k), \kappa_2 + \tan \tau_x \kappa_z) \\ &= \int dx dr W_+(r, x) W_-^*(r + \delta_r, x + \delta_x) \exp[i r (\kappa_r + 2\delta k)] \exp[i \tan \tau_x \kappa_z x]\end{aligned}\quad (27)$$

where $\tilde{W}_i(\kappa_1, \kappa_2)$ is the Fourier transform of $W_i(r, x)$ defined as

$$\tilde{W}_i(\kappa_1, \kappa_2) = \int dr dx e^{-i(\kappa_1 r + \kappa_2 x)} W_i(r, x)$$

Notice that when two transmitters are used, the only difference in the previous formulas is that k_+ must be replaced by $k_+ + k_-$.

The phase of the interferometric product must be corrected for a range dependent term if $\delta k \neq 0$. The expression derived above also shows the phase biases introduced by errors in alignment, of the two interferometric images, as well as errors introduced by the presence of volumetric scattering.

Assuming that the return power for each pixel is the same at both receivers the correlation coefficient between the two signals is given by

$$\begin{aligned}\gamma &= \frac{|\langle v_+ v_-^* \rangle|}{\sqrt{\langle |v_+|^2 \rangle \langle |v_-|^2 \rangle}} \\ &= \frac{|\tilde{\sigma}_0| |\Gamma(\kappa_r + 2\delta k, \kappa_z \tan \tau_x, \delta_r, \delta_x)|}{\tilde{\sigma}_0 |\Gamma(0, 0, 0, 0)|} \frac{1}{\sqrt{1 + \text{SNR}_1^{-1}} \sqrt{1 + \text{SNR}_2^{-1}}} \equiv \gamma_Z \gamma_G \gamma_N \quad (28)\end{aligned}$$

where SNR_i is the i 'th system's signal to noise ratio. The correlation is the product of a geometric correlation function, γ_G , which is purely a function of the shape of the pixel illumination function and the registration error, a correlation function, γ_Z , which depends on the vertical distribution of scatterers, and a correlation function, γ_N which is purely a function of the thermal noise. Notice that in principle γ_G and γ_N can be determined through calibration and from the estimated topography. This means that, if the complex correlation (including phase) is measured, the complex correlation γ_Z can be determined up to an overall phase and, since it is proportional to the Fourier transform of the vertical distribution of scatterers, this distribution can be recovered if enough incidence angles and baselines are obtained. A more detailed analysis of this inversion will be presented elsewhere.

Notice that, in principle, multiplicative noise factors, such as the phase noise due to the sidelobes of other targets (ISLR or integrated sidelobe ratio noise) are automatically included in γ_G if the surface is homogeneous. In practice, scene inhomogeneities or topographic features may introduce additional phase biases and, possibly, decorrelation. This situation will be treated below.

The geometric correlation function is the extension of the usual van Cittert-Zernike theorem [5] to scatterers distributed in three dimensions. As was first noted by Zebker and Villasenor [6], when the carrier frequency is the same for both receivers, the geometric correlation coefficient is proportional to the convolution of the Fourier transform of the two point target response functions. The source of the geometric decorrelation term is the fact that the speckle observed at different angles is decorrelated.

Gatelli *et al.* [1] first proposed that the same speckle pattern could be obtained at two different angles by requiring that the projected wavenumber on the surface be constant. This results in points at the same height having the same interferometric phase difference (but different slant range). This is seen from equation (27), which shows that maximum correlation is achieved when $\delta_r = \delta_x = 0$ and $\kappa_r = -2\delta k$. Neglecting the effects of surface tilt, and misregistration, when this condition is satisfied the geometric correlation factor in equation (28) is equal to one and the only contributors to the phase noise are γ_Z and γ_N . An additional advantage of making this choice is that misregistration in range will not induce any height errors. In fact, we show in Appendix C that when $\kappa_r = -2\delta k$ these advantages will persist in the presence of an arbitrary distribution of surface scatterers. Although these considerations show that selecting two frequencies is desirable, it is impossible to match the frequency difference across an image since the projected wavenumber changes as a function of range. In practice, one must subdivide the scene into segments for which the match is adequate.

To implement the procedure proposed by Gatelli *et al.* [1] given a single transmit bandwidth, one must truncate the spectra of the two received signals to synthesize a carrier frequency difference. This spectral truncation will result in a degradation of the resolution in the range direction. When the amount of spectral overlap (defined as $1 - \kappa_r / \Delta k$, where Δk is the transmit wavenumber bandwidth) is small, this may result in a significant degradation in the achievable range resolution. As an alternative to this procedure, one may apply a window to the return spectrum. This will reduce the point target response (ptr) sidelobes, at a modest cost in the range resolution, thus increasing the geometric correlation. In Appendix D we study the optimal windowing function and show that, when the spectral overlap is close to one, it is given by half a cycle of a cosine function. A comparison of the correlation properties of various windowing functions is presented in figure 3. This figure shows that when the spectral overlap is large, windowing the data can significantly increase the correlation, while, for small spectral overlaps, it is better not to apply any windowing.

The results shown in figure 3 were obtained assuming an ideal point target response, in practice, SAR processors will produce responses with features which are not present in the ideal case: the range and cross-range sidelobes will decay at a slower rate; perfect compression will not be achieved resulting in the presence of energy in directions different from the range and cross range; finally, due to finite sampling restrictions, ambiguities

will appear away from the main peak. Figure 4 presents a typical point target response obtained by simulation of the JPL TOPSAR system [7] after compression with a seismic migration processor [8]. All of the effects mentioned above are apparent in this figure. Using equation (28), one can calculate the correlation properties of the interferometric return, and these are presented in figure 5 for both weighted and unweighted returns. As can be seen, the result of the previous features (which collectively contribute to the ISLR) is to decrease the correlation by an almost constant factor. This is similar to what would be expected if the ISLR contribution were an uncorrelated noise source. The results for a range-Doppler processor such as the one used by Madsen *et al.* [4] are quite similar, although, due to the slightly higher ISLR, there is a small decrease in the correlation.

In order to make a comparison of the relative merits of the approaches presented above, one must take into account the fact that windowing or spectral truncation will increase the geometric correlation but degrade the resolution. If one assumes that all results are averaged to the same resolution by averaging in the range direction, one obtains the following results for the phase noise for the weighted and spectral truncation methods respectively

$$\sigma_{\Phi}^{(W)} = \frac{\sqrt{R(\alpha)} \sqrt{1 - (\gamma_Z \gamma_G^{(W)} \gamma_N)^2}}{\sqrt{2N_L} \gamma_Z \gamma_G^{(W)} \gamma_N} \quad (29)$$

$$\sigma_{\Phi}^{(T)} = \frac{1}{\sqrt{2(1 - \kappa_r/\Delta\kappa)} N_L} \frac{\sqrt{1 - (\gamma_Z \gamma_N)^2}}{\gamma_Z \gamma_N} \quad (30)$$

where $R(\alpha)$ is defined in Appendix C. Figure 6 shows the ratio of the last two variances against the variance for the unweighted, high resolution data. It is clear from these results that the windowing will only significantly improve the phase variance when the SNR and spectral overlap are both high, while it can actually slightly degrade performance for small values of SNR. On the other hand, despite its loss of resolution for small spectral overlaps, the spectral truncation method provides a significant reduction in the phase noise throughout all the parameter space considered here.

The optimum frequency difference is a function of surface slope, which is not known *a priori*, and a degradation in correlation will occur when the actual slope is different to the one used to estimate the frequency difference. To minimize this degradation, one can weight the return spectrum, as discussed above. Since the typical slopes found in natural terrains are not extremely large, so that the spectral overlap remains large, a simple half-cosine weighting should be adequate. Figure 7 shows that for radar parameters typical of airborne radars (15km range, 40 degree incidence angle, 2m baseline, 40MHz bandwidth) this type of weighting can make the geometrical correlation coefficient almost unity for wide range of slopes.

6. Effects Due to Scene Inhomogeneity

The fact that the imaged scene is not homogeneous can introduce errors in the estimated height. Above it was shown that for homogeneous scenes the phase center of the scattering area coincides with the "geometric" phase center (weighted by the volumetric scattering density). This is no longer true for inhomogeneous scenes: sidelobes from a bright part of the scene may leak into darker parts, thus shifting the phase center and inducing errors in the estimated angular elevation of the imaged cell. In Appendix C we show that, when one can arrange that $2\delta k = -\kappa_r$, the height error induced is given by $\langle z \rangle$, i.e. the mean height of all scatterers contributing to a resolution cell weighted by the power they leak into the resolution cell. This simple result is due to the fact that, for $2\delta k = -\kappa_r$, two nearby points will differ in interferometric phase only if they differ in height. This is not true in general since the interferometric phase is a function of look angle and nearby points will have different phases, even if they are at the same height. In this section, we treat the height and position errors for the general case.

A simple estimate of the measurement error for an arbitrary distribution of targets is not available in the general case. Since typical scenes vary mostly in the horizontal direction, we restrict ourselves to an inhomogeneous distribution of scatterers in a plane to obtain an estimate for the magnitude of the position error. From the results derived above, one has that the deviation in the interferometric phase is

$$\delta\Phi = \tan^{-1} \left(\frac{\text{Im}[\tilde{\gamma}]}{\text{Re}[\tilde{\gamma}]} \right) \quad (31)$$

where

$$\tilde{\gamma} = e^{ik_4 \Delta + 2\delta k r_0} \gamma = \frac{\int \sigma(y, x) P(y \sin \theta, x) e^{i(\kappa_r + 2\delta k)y \sin \theta} dS}{\int \sigma(y, x) P(y \sin \theta, x) dS} \quad (32)$$

Here $P \equiv WW^*$ is the point-target response in the power domain, and we have neglected registration errors.

We examine the simplified case of the influence of a single bright point target on an otherwise uniform scene:

$$\sigma(x, y) = \sigma_0 + \sigma_1 \delta(y - y_1) \delta(x - x_1). \quad (33)$$

After integration, the interferometric phase deviation is given by the phase of

$$\tilde{\gamma} = \frac{\sigma_1 P(y_1 \sin \theta, x_1) e^{i(\kappa_r + 2\delta k)y_1 \sin \theta} + \sigma_0 \tilde{P}((\kappa_r + 2\delta k) \sin \theta, 0)}{\sigma_1 P(y_1 \sin \theta, x_1) + \sigma_0 \tilde{P}(0, 0)} \quad (34)$$

where \tilde{P} is the two-dimensional Fourier transform of P . Using $\tilde{P}(0, 0) = 1$ and assuming that $P(y, 0)$ is symmetric and therefore $\tilde{P}(k_y, 0)$ is real, and defining the power of the point

target response multiplied by the ratio of the cross-section of the bright target to that of the background as the "weighted contrast":

$$w(y \sin \theta, x) = 4\pi^2 \frac{\sigma_1}{\sigma_0 \sin \theta} \frac{P(y \sin \theta, x)}{P(\kappa_r + 2\delta k, 0)}, \quad (35)$$

we obtain the interferometric phase deviation as

$$\delta\Phi = \tan^{-1} \left[\frac{\sin((\kappa_r + 2\delta k)y_1 \sin \theta)}{w^{-1}(y_1 \sin \theta, x) + \cos((\kappa_r + 2\delta k)y_1 \sin \theta)} \right] \quad (36)$$

in a side-looking geometry, the height and position errors are

$$\delta h = \frac{\delta\Phi}{\kappa_r} \cos \theta \quad \text{and} \quad \delta y = \delta h / \tan \theta, \quad (37)$$

respectively. When $\kappa_r y \ll 1$, so for nearby bright targets such that $w(y \sin \theta, x) \gg 1$ the positioning errors are approximately:

$$\delta h \approx \frac{w}{1+w} y_1 \sin \theta \cos \theta, \quad \delta y \approx \frac{w}{1+w} y_1 \cos^2 \theta \quad (38)$$

which has a simple geometric interpretation. Define the "phase center" seen by the radar as the aim point weighted by the nearby bright target:

$$y_p = y_1 \frac{w}{1+w}. \quad (39)$$

This function interpolates smoothly between y_1 , the location of the bright target ($w \gg 1$), to zero, the geometric center of the resolution cell ($w \ll 1$). The height measured by the radar is $h = H - r \cos \theta$, where H is the altitude of the radar and r is the range to the target. Then $\delta h = r \sin \theta \delta \theta$. The projection of the displacement of the phase center onto a line perpendicular to the look direction is $y_p \cos \theta = r \delta \theta$, and we have recovered (38).

The height and cross-track errors computed from (36) corresponding to a single bright point target (40 dB above the surrounding terrain) and a sidelooking geometry are plotted in Fig. 8a and b, respectively for a point-target response with a half-cosine range-weighting. The rapid oscillations in the error with range separation from the bright target correspond to the oscillations in the point-target response. The magnitude of the maximum height error as a function of the contrast between the bright target and nearby dim targets is plotted in Fig. 8c. As the brightness of the target increases, the distance from the target at which the maximum height error is incurred increases up to a maximum height error corresponding to a phase deviation of π radians.

The contrast-induced height errors for an extract of a typical rural TOPSAR image have been computed and plotted in Fig. 9. In this case, most of the errors are below the height noise of the image, with the exception of the bright patch to the left of center. The ± 3 meter deviations introduced by this group of bright targets appears to be consistent with the interferometric height map derived from this SAR image.

7. Tropospheric Effects

In the following analysis, we assume that the troposphere is a stratified medium. Earth curvature effects, which may be included with a small additional effort, but which do not significantly alter the results, will be neglected. With these assumptions, the index of refraction n can be modeled as

$$n(z) = 1 + \delta(z) \quad (40)$$

where $\delta(z)$ represents the variation of the index of refraction with height and is typically of order 10^{-4} . An example of this type of model is the Central Radio Propagation laboratory (CRPL) (now NOAA) exponential reference atmosphere [10] which is given by

$$n(z) = 1 + ae^{-z/H} \quad (41)$$

where the conventional values for a and H are taken to be 3.13×10^{-4} and 6.949 km, respectively, when h is the height above sea level.

In Appendix E we show that the relationship between the geometric range r and the path distance \tilde{r} is

$$\tilde{r} = r \left[1 + \frac{1}{3} \left(\frac{7}{6} \left[\left(\frac{r}{\Delta h} \right)^2 - 1 \right] \right) \right] \quad (42)$$

where $\bar{\delta}$ and σ_{δ}^2 , correspond to the height-dependent mean and variance of the variations of the index of refraction, respectively. These two quantities are functions of the height difference between the scatterer and the receiver, Δh , and the height of the scatterer above sea level, h_0 . Figure 10 presents the variation of $\bar{\delta}$ as a function of $\Delta h/H$ for varying h_0 and the CPRL model. Notice that this quantity varies with height and approaches zero exponentially and that there can be a significant variation if the height of the scatterer changes by a large percent of the atmospheric scale height. The InSAR errors are dominated by fluctuations in this quantity.

To get an estimate of the order of magnitude of the second order quantities, Figure 11 presents the tropospheric variance for the CPRL model, normalized by a^2 . As can be seen, this quantity is always smaller than $\sim 7 \times 10^{-2}$, and the peak value occurs at approximately $h/H = 3$, which, for the CPRL model corresponds to a height of approximately 21 km. For typical airplane altitudes between 7 and 14 km, it varies approximately between 3×10^{-2} to 6×10^{-2} . Figure 12 presents the variation of the factor $\sim a \tan 2\theta$ for incidence angles varying from 20 to 80 degrees, in 10 degree steps. Assuming that $a^2 \sim 10^{-7}$, this implies that the peak fractional difference varies approximately between 10^{-9} to 10^{-7} from 20 to 80 degrees. For a slant range of 15 km, this corresponds to a difference between 0.015111111 to 1.5 mm. This becomes approximately one order of magnitude larger for spaceborne platforms. Thus, the effects due to departures from a straight line path and variations in the speed of light inside the medium are extremely small.

One may solve for the geometric range in terms of the electromagnetic range. To second order in δ , the result is

$$r = \frac{\tilde{r}}{1 + \bar{\delta} - \frac{1}{2}\sigma_\delta^2 \left[\left(\frac{\tilde{r}}{\Delta h} \right)^2 - 1 \right]} \quad (43)$$

Notice that this equation involves the height above the target, Δh , and the height of the target above sea level, which are not known *a priori*. Figure 10 shows that, a 10% variation in h_0/H corresponds roughly to a 10% variation in δ , which implies a $\sim 10^{-5}$ variation in the average speed of light. Assuming a 15km range, this produces a range error on the order of 15cm, which is adequate for most topographic applications. If greater accuracy is desired, or if the surface height is known to lesser accuracy, it is necessary to iterate the topographic estimation process to obtain better estimates for h_0 .

From equation (2), the effect of the troposphere on the Doppler frequency is equivalent to replacing the wavenumber by an effective wavenumber

$$\tilde{k} = \frac{d\tilde{r}}{dr} k \quad (44)$$

Using the results derived above, one gets

$$\frac{d\tilde{r}}{dr} = 1 + \bar{\delta} + \sigma_\delta^2 \left[\frac{1}{2} - \frac{3}{2} \left(\frac{r}{\Delta h} \right)^2 \right] \quad (45)$$

Again, thin-c is a first order effect due to the average speed of light in the medium, and a second order term due to ray bending and differential delays. The change in Doppler frequency depends, to first order, on the height of the target above sea level. Therefore, to get an exact solution, an iterative approach is necessary. However, for most applications, taking a reference height may be sufficient.

Assuming that the interferometric antennas are located at a heights h and $h + \delta h$, the electromagnetic path length to the second antenna as a function of the corresponding geometric distance r_- is given by

$$\tilde{r}_- = r_- \left[1 + \bar{\delta} + \left(\Delta h \frac{\partial \bar{\delta}}{\partial h} \right) \frac{\delta h}{\Delta h} - \frac{1}{2} \sigma_\delta^2 \left[\left(\frac{r_-}{\Delta h + \delta h} \right)^2 - 1 \right] \right] \quad (46)$$

where we have assumed that the atmosphere at the receiver is so tenuous that one can approximate $\bar{\delta}(h + \delta h) \approx \bar{\delta}(h) + \delta h \frac{\partial \bar{\delta}(h)}{\partial h}$.

Using this result, the interferometric phase can be approximated by

$$\Phi \approx -k(r_+ - r_-) \left[1 + \bar{\delta} + \sigma_\delta^2 \left(\frac{1}{2} - \frac{3}{2} \sec^2 \theta \right) \right] + k r_- \left(\Delta h \frac{\partial \bar{\delta}}{\partial h} \right) \frac{\delta h}{\Delta h} \quad (47)$$

We see that the changes in the interferometric phase are almost identical to the changes in the Doppler frequency (modulo factors proportional to $(B/h)^2$), and the comments made

above apply as well. However, these expressions now involve an additional term which is proportional to the fractional change in the speed of light due to the fact that the two antennas are not located at the same height. At first sight, this term might appear to be negligible. However, since it is multiplied by a large factor of kr' , this is not always the case. One can rewrite the derivative term as

$$\left(\Delta h \frac{\partial \delta}{\partial h} \right) \frac{\delta h}{\Delta h} = (\delta(h) - \bar{\delta}) \frac{\delta h}{\Delta h} \quad (48)$$

Figure 13 presents a graph of $(\delta(h) - \bar{\delta})/a$ for the CPRL model atmosphere (solid line). It can be seen that, because the factor kr' is typically on the order of 10^6 for airborne situations, one cannot ignore the additional term in estimating the interferometric phase since it is of the same order of magnitude as the effect of the speed of light. The dashed line is a plot of $-\bar{\delta}/a$, which describes the behaviour of the derivative for $h/H > 3$. On the other hand, for $h/n < 3$, as is the case for most airborne situations, the local index of refraction plays an important role in determining the value of the derivative. In a turbulent atmosphere, or near the envelope of the airplane, this quantity may fluctuate significantly from its model prediction. The dash-dotted lines in Figure 13 represent the effect of a 10% variation of the local index of refraction on the derivative term. As can be seen, while the effect is perceptible, the difference is an order of magnitude smaller than the model correction term. One concludes that making a correction to the interferometric phase based on a model atmosphere is good to order δ , and that atmospheric turbulence will introduce effects to order δ^2 or higher.

Given \hat{r}_+ , \hat{r}_- , Φ , and f_D , using the relationship $\vec{r}_{\pm} = \vec{r} \pm \vec{B}/2$ together with equations (43), (45), and (46), one can solve equations (5) and (6) exactly (assuming a value of h) to obtain $\hat{n} \cdot \vec{B}$ and $\hat{n} \cdot \vec{v}$, although this involves solving a cubic equation. By enforcing the condition that \hat{n} be a unit vector, one can then solve for it and obtain a solution for the height of the target by using equation (4). The equations can then be iterated to obtain higher accuracy. However, given the fact that the errors are dominated by uncertainties in the speed of light, this may be unnecessarily complicated. A simpler procedure, if the target height is known to an adequate accuracy, is to assume nominal values for \vec{r}_{\pm} , h and for $\hat{n} \cdot \vec{B}$ in the second order terms, and to solve the equations without iterations. The solution is then identical to the solution neglecting the troposphere, the only difference being that the wavenumber is scaled with a factor which may depend on the angle of incidence, and an additional correction must be applied when the baseline is not horizontal. If additional accuracy is required, Δh is estimated from a first iteration of the topographic map, and from this estimate a value for δk , the error in the wavenumber, is derived. Finally, a correction is made to the map heights and locations using equation (12) to estimate the correction vector.

8. Conclusions

We have presented a systematic evaluation of the error sources for an airborne interferometric system and derived formulas for the sensitivity of the interferometric positioning error to each source. The most important consequences of these analyses can be summarized as follows:

1. in order to minimize various InSAR errors, it is advantageous to place the interferometric baseline as perpendicular as possible to the look direction.
2. To reduce positioning errors, it is advantageous to place the look direction, the baseline direction, and the vertical axis on the same plane.
3. To reduce phase noise and leakage due to scene contrast, one must use a two-frequency system such as the one proposed by Gatelli *et al.* [1].
4. It is necessary to make corrections to both the Doppler frequency and the interferometric phase to account for delays due to tropospheric propagation. However, if the surface height is known to adequate accuracy, these corrections are simple to incorporate into the standard InSAR processing scheme. The largest effect will be accounted for merely by using the average speed of light in the medium.

Appendix A

Interferometric Sensitivities

Phase Sensitivity:

If one decomposes the baseline into a component, $\vec{B}_{||}$, parallel to the velocity direction, \hat{v} , and a component, $\vec{B}_{\perp} = (1 - \hat{v}\hat{v}) \cdot \vec{B}$ perpendicular to it, then from equation (11) and equation (5), one has

$$\delta \hat{n} \cdot \hat{\beta} = \frac{\delta \tilde{\Phi}}{B_{\perp}} \quad (49)$$

where $\hat{\beta}$ is a unit vector perpendicular to \hat{v} and defined by $\hat{\beta} = \vec{B}_{\perp} / B_{\perp}$. Defining a last unit vector $\hat{\gamma} \equiv \hat{\beta} \times \hat{v}$, the component of the position error along this direction due to a phase error can be obtained by using equation (8)

$$\delta \hat{n} \cdot \hat{\gamma} = -\frac{\hat{n} \cdot \hat{\beta}}{\hat{n} \cdot \hat{\gamma}} \delta \hat{n} \cdot \hat{\beta} = -\frac{\hat{n} \cdot \hat{\beta}}{\hat{n} \cdot \hat{\gamma}} \frac{\delta \tilde{\Phi}}{B_{\perp}} \quad (50)$$

Baseline Sensitivity

From equation (5) one has that, in the presence of baseline errors,

$$\delta \hat{n} \cdot \vec{B} = -\hat{n} \cdot \delta \vec{B} \quad (51)$$

Since baseline errors are independent of velocity, one deduces from this equation that

$$\delta \hat{n} \cdot \hat{\beta} = -\hat{n} \cdot \frac{\delta \vec{B}}{B_{\perp}} \quad (52)$$

$$\delta \hat{n} \cdot \hat{v} = 0 \quad (53)$$

Finally, using equation (8) one has again

$$\delta \hat{n} \cdot \hat{\gamma} = -\frac{\hat{n} \cdot \hat{\beta}}{\hat{n} \cdot \hat{\gamma}} \delta \hat{n} \cdot \hat{\beta} = \frac{\hat{n} \cdot \hat{\beta}}{\hat{n} \cdot \hat{\gamma}} \hat{n} \cdot \frac{\delta \vec{B}}{B_{\perp}} \quad (54)$$

Velocity Sensitivity

From equation (11)

$$\delta \hat{n} \cdot \hat{v} = -\hat{n} \cdot \frac{\delta \vec{v}}{v} \quad (55)$$

Also, from equation (51), one has

$$\delta \hat{n} \cdot \vec{B} = B_{\perp} \hat{\beta} \cdot \delta \hat{n} + B_{\parallel} \hat{v} \cdot \delta \hat{n} = 0 \quad (56)$$

Together with equation (11), this implies

$$\hat{\beta} \cdot \delta \hat{n} = \frac{B_{\parallel}}{B_{\perp}} \hat{n} \cdot \frac{\delta \vec{v}}{v} \quad (57)$$

The final component is obtained by using equation (8)

$$\begin{aligned} \delta \hat{n} \cdot \hat{\gamma} &= \frac{-1}{\hat{n} \cdot \hat{\gamma}} \left((\hat{n} \cdot \hat{\beta}) \delta \hat{n} \cdot \hat{\beta} + (\hat{n} \cdot \hat{v}) \delta \hat{n} \cdot \hat{v} \right) \\ &= \frac{1}{\hat{n} \cdot \hat{\gamma}} \left(\hat{n} \cdot \hat{v} - \frac{B_{\parallel}}{B_{\perp}} \hat{n} \cdot \hat{\beta} \right) \hat{n} \cdot \frac{\delta \vec{v}}{v} \end{aligned} \quad (58)$$

Notice that, as expected, the only part of the baseline and velocity errors which matter are the component of the errors in the ii direction.

Wavenumber Sensitivity

From equation (6), it follows that

$$\delta \hat{n} \cdot \hat{v} = -\hat{n} \cdot \hat{v} \frac{\delta k}{k} \quad (59)$$

Similarly, from equation (5), it follows that

$$\delta \hat{n} \cdot \hat{\beta} = -\hat{n} \cdot \hat{\beta} \frac{\delta k}{k} \quad (60)$$

Finally, using equation (8),

$$\delta \hat{n} \cdot \hat{\gamma} = \left(\frac{1}{\hat{n} \cdot \hat{\gamma}} - \hat{n} \cdot \hat{\gamma} \right) \frac{\delta k}{k} \quad (61)$$

The previous equations may be summarized in one vector equation. Defining the unit vector along the baseline direction as $\hat{b} = \vec{B}/B$, one can write the position error as

$$\delta \vec{r}_g = \delta \vec{r}_a + \hat{n} \delta r + r \frac{\hat{n} \times \hat{v}}{\hat{b} \cdot (\hat{n} \times \hat{v})} \left[\frac{\delta \tilde{\Phi}}{B} - \hat{n} \cdot \frac{\delta \vec{B}}{B} \right] + r \frac{\hat{n} \times \hat{b}}{\hat{b} \cdot (\hat{n} \times \hat{v})} \hat{n} \cdot \frac{\delta \vec{v}}{v} + r \left[\frac{\hat{v} \times \hat{b}}{\hat{b} \cdot (\hat{n} \times \hat{v})} - \hat{n} \right] \frac{\delta k}{k} \quad (62)$$

Appendix B

Model the interferometric signal by a set of N_L pairs of SAR returns, $\{v_+^{(k)}, v_-^{(k)}\}_{k=1}^{N_L}$, where elements in the pair represent the voltage returns from the same resolution element viewed by each of the InSAR antennas. We assume the signal has the following correlation properties:

$$\langle v_+^{(k)} v_+^{*(l)} \rangle = \delta_{kl} (P_k + N) \quad (63)$$

$$\langle v_-^{(k)} v_-^{*(l)} \rangle = \delta_{kl} (P_k + N) \quad (64)$$

$$\langle v_+^{(k)} v_-^{*(l)} \rangle = \delta_{kl} (P_k \gamma_{Gk} e^{i\Phi}) \quad (65)$$

where P_k is the signal power, N is the thermal noise power, $0 \leq \gamma_{Gk} \leq 1$, and Φ is the interferometric phase, which is the parameter to be estimated. Notice that it is assumed that the interferometric phase Φ is the same for all signal pairs. This implies that the resolution elements to be averaged have the same height and are located along isophase lines (which correspond to the along track direction for a flat surface). Notice also that the mean power is allowed to vary from resolution element to resolution element, as is the magnitude of the field correlation coefficient. This allows for the possibility of averaging different resolution elements whose intrinsic brightness and intrinsic roughness may not be the same. In this case, the upper index labels the resolution element. On the other hand, one may gain independent samples by overlaying independent looks of the same resolution element. In this case, the upper index labels the independent looks, and P_k and γ_{Gk} are constant from look to look.

The correlation coefficient for any interferometric pair ($k=l$) is given by

$$\frac{\langle v_+^{(k)} v_-^{*(k)} \rangle}{\langle v_+^{(k)} v_+^{*(k)} \rangle} \equiv \frac{\text{SNR}_k \gamma_{Gk} e^{i\Phi}}{1 + \text{SNR}_k} \equiv \gamma_k e^{i\Phi} \quad (66)$$

Define χ_k as

$$\chi_k = (4, v_-^{(k)}) C_k^{-1} (v_+^{*(k)}, v_-^{*(k)})^T \quad (67)$$

$$= \frac{|v_+^{(k)}|^2 + |v_-^{(k)}|^2}{(P_k + N)(1 - \gamma_k^2)} - \frac{\gamma_k e^{-i\Phi} v_+^{(k)} v_-^{*(k)}}{(P_k + N)(1 - \gamma_k^2)} = \frac{\gamma_k e^{i\Phi} v_+^{*(k)} v_-^{(k)}}{(P_k + N)(1 - \gamma_k^2)} \quad (68)$$

where C_k^{-1} is the inverse of the correlation matrix for $v_+^{(k)}$ and $v_-^{(k)}$. Define also

$$\chi = \sum_{k=1}^{N_L} \chi_k \quad (69)$$

After all these definitions, we are ready to prove the main result of this Appendix:

Lemma: Let $f(v_+^{(1)}, v_-^{(1)}, \dots, v_+^{(N_L)}, v_-^{(N_L)} | \Phi)$ be a conditional probability function for the interferometric observations given the interferometric phase difference Φ . If

1. the only dependence of f on Φ is through a function of χ
2. f is a strictly monotonically decreasing function of χ

the maximum likelihood estimator for Φ is given by

$$\hat{\Phi} = \text{Arg} \left[\sum_{k=1}^{N_L} \frac{\gamma_k v_+^{(k)} v_-^{*(k)}}{(P_k + N)(1 - \gamma_k^2)} \right] \quad (70)$$

For the case in which all the pixel pairs have the same statistics, this reduces to

$$\hat{\Phi} = \arctan \left(\frac{\text{Im} \sum_{k=1}^{N_L} v_+^{(k)} v_-^{*(k)}}{\text{Re} \sum_{k=1}^{N_L} v_+^{(k)} v_-^{*(k)}} \right) \quad (71)$$

which is the estimator used by Li and Goldstein [2].

Proof: The maximum likelihood estimate for Φ is given by solving the equation

$$\frac{\partial}{\partial \Phi} f(v_+^{(1)}, v_-^{(1)}, \dots, v_+^{(N_L)}, v_-^{(N_L)} | \Phi) = 0 \quad (72)$$

provided f is a maximum (not a minimum) at this point. Because of assumption (1), this can be written as

$$\frac{\partial f}{\partial \chi} \frac{\partial \chi}{\partial \Phi} = 0 \quad (73)$$

From assumptions (2), and since f is a pdf and χ is a biquadratic form (which implies $\chi = 0$ iff $|v_+^{(k)}|^2 = |v_-^{(k)}|^2 = 0 \forall k$, which is not an interesting case since it implies the absence of a return signal), this condition reduces to

$$\frac{\partial}{\partial \Phi} \chi = i \left(e^{-i\hat{\Phi}} \sum_{k=1}^{N_L} \frac{\gamma_k v_+^{(k)} v_-^{*(k)}}{(P_k + N)(1 - \gamma_k^2)} - \text{complex conjugate} \right) = 0 \quad (74)$$

This is easily solved for $\hat{\Phi}$ to obtain

$$\hat{\Phi} = \text{Arg} \left[\sum_{k=1}^{N_L} \frac{\gamma_k v_+^{(k)} v_-^{*(k)}}{(P_k + N)(1 - \gamma_k^2)} \right] \quad (75)$$

in the case where all the pixel pairs have the same statistics, this reduces to

$$\hat{\Phi} = \arctan \left(\frac{\text{Im} \sum_{k=1}^{N_L} v_+^{(k)} v_-^{*(k)}}{\text{Re} \sum_{k=1}^{N_L} v_+^{(k)} v_-^{*(k)}} \right) \quad (76)$$

which is the promised result. Due to speckle, the mean power cannot be determined for individual pixels, and, in practice, one always assumes that all the pixels in a multi-look image have the same statistics. In this case, the last formula is the correct one to apply. However, if enough looks are taken, or if *a priori* information exists, one may be able to make use of the previous formula.

The two relevant pdf's for radar scattering speckle are the circular Gaussian

$$f = \frac{1}{(2\pi)^2 |C|^{1/2}} \exp(-\chi) \quad (77)$$

and the multivariate K distribution [9]

$$f = \frac{1}{(2\pi)^2 |C|^{1/2}} \frac{(2\alpha)^{1+\alpha/2} \chi^{\alpha/2-1}}{2^{\alpha-1} \Gamma(\alpha)} K_{2-\alpha}(\sqrt{2\alpha\chi}) \quad (78)$$

It is well known that both of these distributions satisfy the conditions required by the lemma.

As an interesting consequence of this result, one can derive the asymptotic value of the estimated phase standard deviation if the return voltage signal is circular Gaussian distributed. It is well known [11] that a maximum likelihood estimator approaches the Cramer-Rao bound asymptotically and its variance is given by

$$\text{var}(\hat{\Phi}) = \frac{1}{N_L J} \quad (79)$$

where J is defined by

$$J = -\left\langle \frac{\partial^2}{\partial \Phi^2} \ln f(v_+^{(i)}, v_-^{(i)} | \Phi) \right\rangle \quad (80)$$

If the pixel pair statistics are uniform over the scene, then J is easily computed. The final result for the estimated phase standard deviation, σ_Φ , is given by the simple formula

$$\sigma_\Phi = \frac{1}{\sqrt{2N_L}} \frac{\sqrt{1-\gamma}}{\gamma} \quad (81)$$

Notice that, strictly speaking, these equations apply to the unwrapped phase; i.e. the 2π ambiguity in the phase estimation is assumed to have been removed. When this ambiguity is still present, the phase noise standard deviation will saturate as the phase becomes uniformly distributed in the interval $[0, 2\pi]$. Equation (81) applies when $\sigma_\Phi \ll \pi$, which is the normal situation in interferometry.

Appendix C

When $2\delta k = -\kappa_r$ and for zero slopes, one may rewrite equation (18) using equation (20) as

$$\langle v_+ v_-^* \rangle = |A|^2 \exp[-ik_+ A] \exp[-i2\delta k r_0] \int dx dy dz \sigma_0(x, y, z) \exp[-i\kappa_z z] W_+(r_0 + A/2 - r_+) W_-^*(r_0 - A/2 + \delta_r - r_+, x_0 + \delta_x - x) \quad (82)$$

where, aside from the exponential, all the terms inside the integral are real functions. Hence it follows that, if all the scatterers are in a $z = z_0$ constant plane, the only contribution to the interferometric phase is a constant phase factor $\exp[i\kappa_z z_0]$, which corrects the phase difference for the geometric height shift in the scatterers. Notice that there is no phase contribution due to a relative misalignment of the two point target response functions.

in typical interferometric applications, one has that $\kappa_z z \ll 1$ and one may approximate $\exp[-i\kappa_z z] \approx 1 - i\kappa_z z$. In this case, one can derive a simple and intuitive formula for the additional phase shift due to an arbitrary scatterer distribution. For small phase errors, $\delta\Phi$ is approximately given by the ratio of the imaginary to the real parts of the integral above. A simple calculation shows that this is given by

$$\delta\Phi = -\kappa_z \langle z \rangle \quad (83)$$

where $\langle z \rangle$ is the average height of all the scatterers weighted by their magnitude and the magnitude of their contribution to the resolution cell; i.e.,

$$\langle z \rangle = \frac{\int dx dy dz z [\sigma_0(x, y, z) W_+(r_0 - r_+) W_-^*(r_0 - \Delta + \delta_r - r_+, x_0 + \delta_x - x)]}{\int dx dy dz \sigma_0(x, y, z) W_+(r_0 - r_+) W_-^*(r_0 - \Delta + \delta_r - r_+, x_0 + \delta_x - x)} \quad (84)$$

Appendix D

Assume that the ptr is separable into range and cross-range components, that misregistration errors and slopes can be neglected, and that the two ptr's are identical. Under these circumstances, using equations (27) and (28), one can write the geometric correlation as

$$\gamma_G(\tilde{W}, \kappa_r + 2\delta k) = \frac{\int d\kappa W_t \tilde{W}(\kappa - (\kappa_r + 2\delta k)) \tilde{W}(\kappa)}{\int d\kappa \tilde{W}^2(\kappa)} \quad (85)$$

We seek the function \tilde{W} which maximizes γ_G , given a certain bandwidth: i.e. $\tilde{W} = 0$ for $|\kappa| > AK/2$. Taking the first variation of γ_G , and setting it to zero, one obtains the following condition for the optimal weighting function inside the interval $[-AK/2, AK/2]$

$$\tilde{W}(\kappa - (\kappa_r + 2\delta k)) + \tilde{W}(\kappa + (\kappa_r + 2\delta k)) - 2\gamma_G(\tilde{W}, \kappa_r + 2\delta k) \tilde{W}(\kappa) = 0 \quad (86)$$

This is a nonlinear delayed difference equation, which we have not been able to solve analytically. Notice however, that close to the optimum solution $\delta\gamma_G/\delta\tilde{W} = 0$, and the optimal correlation, $\tilde{\gamma}_G$, is approximately independent of \tilde{W} . When $\kappa_r + 2\delta k \ll \Delta\kappa$, one can expand \tilde{W} in powers of $\kappa_r + 2\delta k$ in equation (86) to obtain the following differential equation, valid to second order in the expansion parameter

$$(\kappa_r + 2\delta k)^2 \tilde{W}''(\kappa) + 2 [1 - \tilde{\gamma}] \tilde{W}(\kappa) = 0 \quad (87)$$

Using the boundary conditions mentioned above and normalizing the peak of the weighting function to 1, the optimal solution is given by

$$\tilde{W}(\kappa) = \cos \frac{\pi \kappa}{\Delta\kappa} \quad (88)$$

$$\tilde{\gamma} = 1 - \frac{1}{2} \left(\frac{\pi(\kappa_r + 2\delta k)}{\Delta\kappa} \right)^2 \quad (89)$$

While equation (86) cannot be solved analytically, it can be solved numerically by iteration. The numerical optimal solutions consist of discrete frequency bands modulated by a cosine function (which need not be zero at the edges of the bandwidth). For spectral overlaps greater than approximately 0.9, the numerical solutions and correlation coefficients agree very well with the results quoted above. However, while the numerical solutions do maximize the correlation function, due to the presence of discrete frequency bands, the resultant point target responses for spectral overlaps smaller than 0.9 tend to have very large sidelobes, which degrade the resolution to unacceptable levels. As a compromise solution, we seek a weighting function of the form

$$\hat{W}(\kappa) = \cos \frac{\alpha \pi \kappa}{\Delta\kappa} \quad (90)$$

and obtain α by optimizing γ_G numerically. The resultant values of α as a function of the spectral overlap are presented in Figure 14. As can be seen, the optimal spectral window transitions from the solution obtained above for large spectral overlaps to an unweighed solution when the spectral overlap is smaller than about 0.5. In Figure 3, we present the geometric correlation function for several weighting functions, including, in addition, the popular Hamming and Hanning weighting functions. As can be seen, for large spectral overlaps, the use of a weighting function can significantly increase the correlation, while no weighting is preferable for smaller spectral overlaps. Notice also that the optimal window proposed here has a resulting (unnormalized) point target response given by

$$W(r) = \text{sinc} \left(\frac{\Delta\kappa r}{2} - \frac{\alpha\pi}{2} \right) + \text{sinc} \left(\frac{\Delta\kappa r}{2} + \frac{\alpha\pi}{2} \right) \quad (91)$$

whose Rayleigh (peak-to-null) resolution can be shown to be given approximately by $2\pi(1 + 0.4(\alpha^2 - \alpha^3) + \alpha^4/2)/\Delta\kappa \equiv 2\pi R(\alpha)/\Delta\kappa$. This implies a degradation in resolution by a factor

of $(1 + \alpha/2)$ relative to the unweighted response. This level of degradation is smaller than that resulting from using either Hamming or Hanning weighting, since these two weighting functions have a smaller effective bandwidth than the simple cosine function considered here.

Appendix E

A straightforward application of Snell's law results in the following two expressions for the geometric incidence angle θ and the electromagnetic path length, \hat{r} , as a function of the height of the platform, h , the incidence angle of the propagating ray at the platform, θ_0 , and the index of refraction at the platform, n_0 :

$$\tan \theta = \frac{\sin \theta_0}{Ah} \int_{h_0}^h dz \frac{(n_0/n(z))}{\sqrt{1 - (n_0/n(z))^2 \sin^2 \theta_0}} \quad (92)$$

$$\hat{r} = \int_{h_0}^h dz \frac{n(z)}{\sqrt{1 - (n_0/n(z))^2 \sin^2 \theta_0}} \quad (93)$$

It is useful to break up the electromagnetic path length into two pieces: r_c , the geometric length of the curved path followed by the ray; and r_d , the additional delay due to the fact that the speed of light in the atmosphere is lower than the speed of light *in vacuo*. These two quantities are given by

$$r_c = \int_{h_0}^h dz \frac{1}{\sqrt{1 - (n_0/n(z))^2 \sin^2 \theta_0}} \quad (94)$$

$$r_d = \int_{h_0}^h dz \frac{n(z) - 1}{\sqrt{1 - (n_0/n(z))^2 \sin^2 \theta_0}} \quad (95)$$

The geometric length differs from the true range only when there is a gradient in the index of refraction and the incidence angle is different from zero; however, the delay length is present even when no ray bending occurs, as is the case of nadir looking altimeters.

The previous equations can be integrated analytically for a few atmospheric profiles, such as the CPRL profile. Instead of specializing to a specific profile, these equations can be integrated in general by expanding in powers of δ . The results are series in terms of the moments of the variations in the index of refraction. Here, terms of order δ^3 and higher will be neglected. This is justified given the magnitude of δ , and given the fact that fluctuations about any given "standard" profile will be larger than this amount. Given this approximation, the integrations yield the following expressions

$$\tan \theta = \tan \tilde{\theta} \left[1 - \sec^2 \tilde{\theta} f_{(1)} + \frac{1}{2} (3 \sec^4 \tilde{\theta} - \sec^2 \tilde{\theta}) f_{(2)} \right] \quad (96)$$

$$r_c = \Delta h \sec \tilde{\theta} \left[1 - \tan^2 \tilde{\theta} f_{(1)} + \frac{3}{2} (\sec^4 \tilde{\theta} - \sec^2 \tilde{\theta}) f_{(2)} \right] \quad (97)$$

$$r_d = Ah \sec \tilde{\theta} [f_{(1)} - \tan^2 \tilde{\theta} f_{(2)}] \quad (98)$$

where $f_{(n)}$ is the n th moment of the variations of the refractive index

$$f_{(n)} = \frac{1}{\Delta h} \int_{h_0}^h dz \delta^n(z) \quad (99)$$

$Ah = h - h_0$, and $\tilde{\theta}$ is the incidence angle at infinity, which is defined by $\sin \tilde{\theta} = n_0 \sin O$. We will also use the abbreviations $\bar{\delta} \equiv f_{(1)}$ and $\sigma_\delta^2 \equiv f_{(2)} - \bar{\delta}^2$, corresponding to the mean and variance of the variations of the index of refraction, both of which are functions of height.

Notice that equations (96), (97), and (98) predict that the change in incidence angle and range relative to the straight line path are first order in δ , and "thus potentially large for large incidence angles and ranges. However, it is not these quantities that are of relevance to the location of the target. Rather, it is the geometric range and incidence angles to the target which are important. In this appendix, equations (96), (97), and (98) are inverted (to second order in δ) to obtain a solution for the geometric range as a function of the measured range.

Expanding the incidence angle at infinity

$$\tilde{\theta} = \tilde{\theta}_0 + \tilde{\theta}_1 + \tilde{\theta}_2 + \dots \quad (100)$$

assuming that $\tilde{\theta}_n$ is of order δ^n , inserting the results into equation (96), solving order by order, and replacing the results in equations (97) and (98), one obtains the following simple expression for the path distance as a function of the geometric incidence angle

$$r_c = \Delta h \sec \theta \left[1 + \frac{1}{2} \sigma_\delta^2 \tan^2 \theta \right] \quad (101)$$

$$r_d = \Delta h \sec \theta \left[\bar{\delta} - \sigma_\delta^2 \tan^2 \theta \right] \quad (102)$$

The first equation shows that the ray curvature adds an additional distance to the propagation, but this distance is second order in δ . Recalling that $\sec \theta = T/Ah$, one obtains the relationship between the geometric range r and the path distance \tilde{r}

$$\tilde{r} = r \left[1 + \bar{\delta} - \frac{1}{2} \sigma_\delta^2 \left[\left(\frac{r}{\Delta h} \right)^2 - 1 \right] \right] \quad (103)$$

This result shows that the difference between the geometric distance and the path distance is due to two effects: to first order, there is a constant scaling factor which accounts for the fact that the average speed of light in the atmosphere is slower than the speed of light *in vacuo*. In addition to this, there are second order corrections which are due to the increase in path length due to ray bending, and to the variations in the speed of light in the presence of variations in the index of refraction. Both second order effects are proportional to the variance of the height dependent part of the index of refraction.

Acknowledgement

The research described in this paper was carried out by the Jet Propulsion laboratory, California institute of Technology, under contract with the National Aeronautics and Space Administration. We would particularly like to thank J .M. Martin for comments and corrections. We would also like to thank S.Hensley, J. Martin, P. Rosen, and H.Zebker for fruitful discussions.

References

- [1] Gatelli, F., Monti Guarnieri, A., Parizzi, F., Pasquali, P., Prati, C., Rocca, F., "Use of the spectral shift in SAR interferometry: applications to ERS-1," submitted to IEEE Trans. Geoscience and Rem. Sen., 1993.
- [2] Li, H. K., and R. Goldstein, "Studies of multibaseline spaceborne interferometric synthetic aperture radars," IEEE Trans. Geoscience and Rem. Sen., vol. 28, no. 1, 1990.
- [3] Rodriguez, E., Martin, J. M., "Theory and design of interferometric synthetic aperture radars," IEEE Proc.-F, 139, no. 2, 147-159, 1992.
- [4] Madsen, S. N., Zebker, H. A., Martin, J. M., "Topographic mapping using radar interferometry: processing techniques," IEEE Trans. Geoscience and Remote Sensing, 31, no. 1, 246-256, 1993.
- [5] Goodman, J.W., "Statistical optics," Wiley-Interscience, New York, 1985.
- [6] Zebker, H. A., Villasenor, J., "Decorrelation in interferometric radar echoes," IEEE Trans. Geoscience and Rem. Sen., 30, no. 5, 950-959, 1992.
- [7] Zebker, H. A., Madsen, S. N., Martin, J. M., Wheeler, K., "The TOPSAR interferometric radar topographic mapping instrument," IEEE Trans. Geoscience and Rem. Sen., 30, no. 5, 933-940, 1992.
- [8] Prati, C., F. Rocca, A. Monti Guarnieri, E. Damonti, "Seismic migration for SAR focusing: interferometric applications," IEEE Trans. Geoscience and Remote Sensing, 28, 627-639, 1990.
- [9] Yeh, S.H., Kong, J. A., Jao, J. K., Shin, R.T., Novak, L. M., "K-distribution and polarimetric terrain radar clutter," J. Electr. Waves and Appl., in press
- [10] Blake, L.V., "Radar Range-Performance Analysis," Artech House, Inc., 1986.
- [11] Sorenson, H.W., "Parameter Estimation," Marcel Dekker, Inc., 1980.

Figure Captions

Figure 1: InSAR geometry.

Figure 1: Phase standard deviation as a function of the number of looks for the simulated results (solid line) and the maximum likelihood prediction (dashed line). The correlation coefficients used were 0.99 (crosses), 0.9 (diamonds), 0.8 (squares), and 0.6 (triangles).

Figure 3: Correlation function for different range range windows: No weighting (solid line); half-cosine weighting (dashed line); banning weighting (dashed-dotted line); hamming weighting (dotted line); optimum cosine weighting (small triangles).

Figure 4: Point target response for the TOPSAIL instrument using a range migration processor. Note the azimuth ambiguities.

Figure 5: Correlation function using the two-dimensional point target response for no weighting (a) and half-cosine weighting (b). The dashed line is the response expected for an ideal one-dimensional unweighed point target response.

Figure 6: Phase noise relative to an unweighted point target response for an optimal cosine weighting (a) and the spectral truncation method of Gatelli *et al.* [1].

Figure 7: Geometric correlation coefficient for the two frequency technique as a function of local surface slope. The solid line is for an unweighed spectrum, the dashed line for half-cosine weighting. The radar parameters are given in the text.

Figure 8: Errors in height (a) and positioning (b) for a single point target 40dB brighter than the background as a function of distance from the point target, (c) Plots the maximum height error for varying contrast values.

Figure 9: SAR contrast image (a) for an agricultural area, including fields and two roads. The corresponding height error is plotted in (b). A corresponding cut through the highest contrast area is shown in (c) and (d). Notice that only contrast differences in the azimuth direction (up-down) give rise to height errors,

Figure 10: Variation of $\bar{\delta}$ as a function of h/lf for the CPRL model.

Figure 11: Tropospheric variance for the CPRL model, normalized by α^2 .

Figure 12: Variation of the factor $\frac{1}{2}\sigma_{\delta}^2 \tan^2 \theta$ for incidence angles varying from 20 (lowest curve) to 80 degrees (highest curve), in 10 degree steps.

Figure 13: Plots of $(\delta(h) - \bar{\delta}(h))/\alpha$ model atmosphere (solid line) and $-\bar{\delta}(h)/\alpha$ (dashed line) for the CPRL. The dashed-dotted lines represent the effect of a 10% variation of the local index of refraction.

Figure 14: Optimum value of the parameter a for spectral weighting as a function of the amount of spectral overlap.

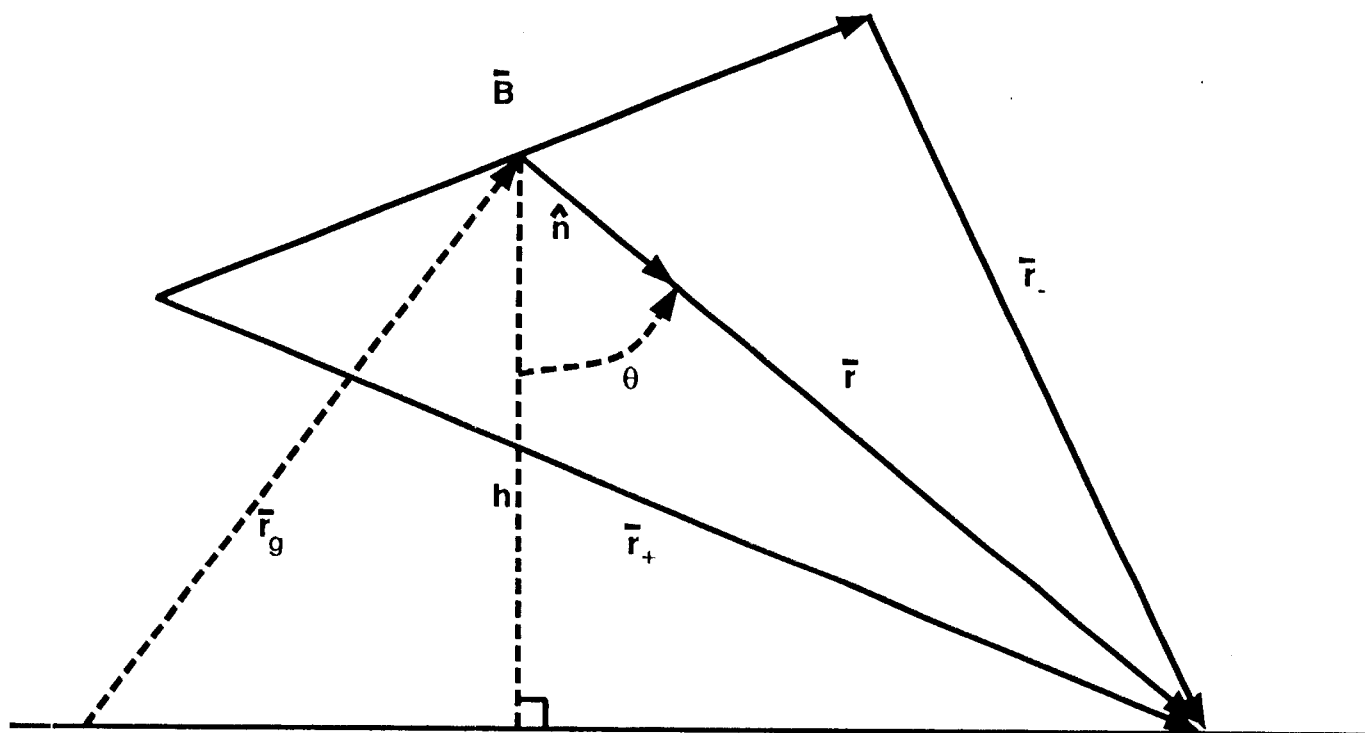
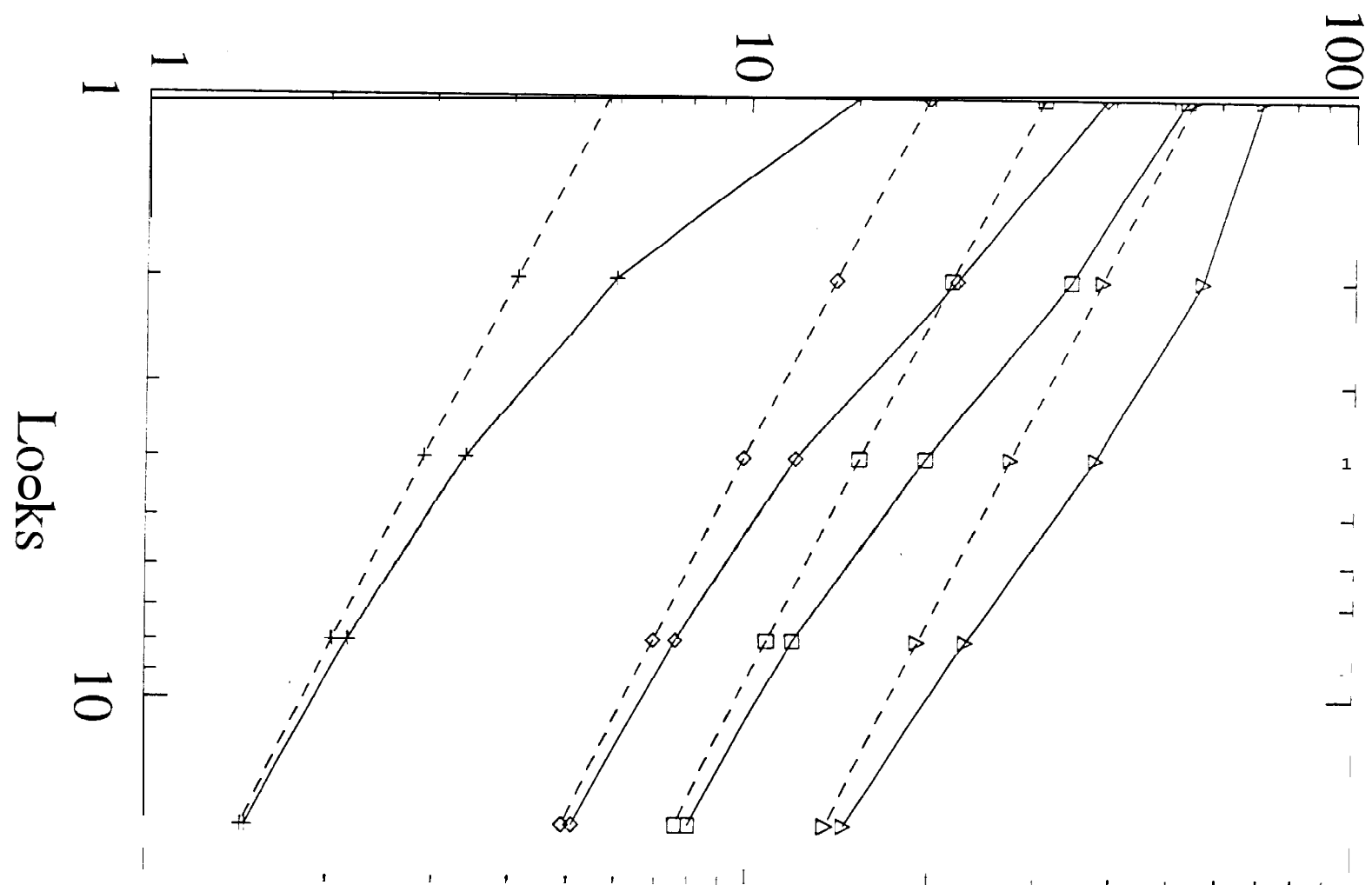
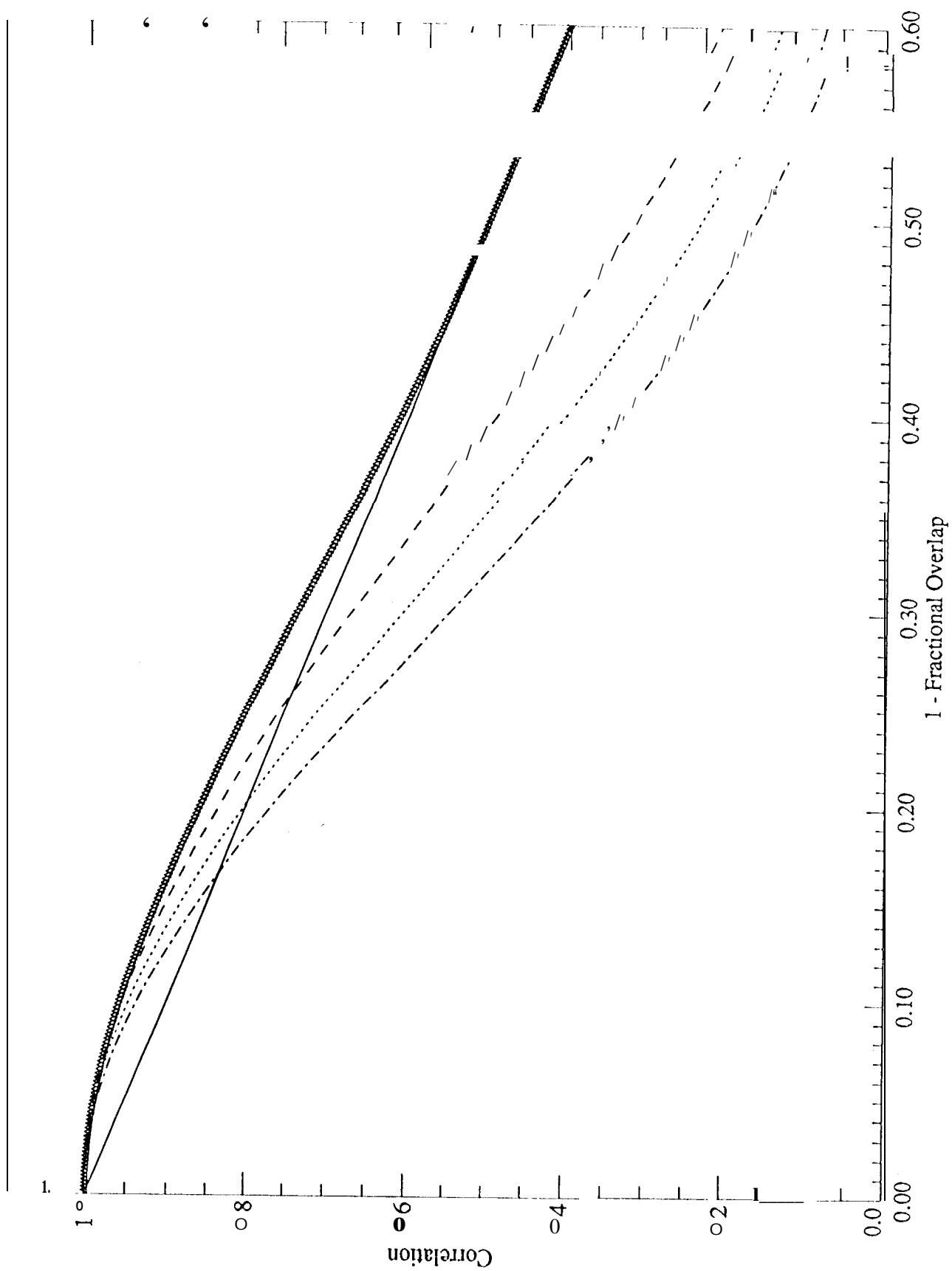


Figure 1

Phase Standard Deviation (deg)





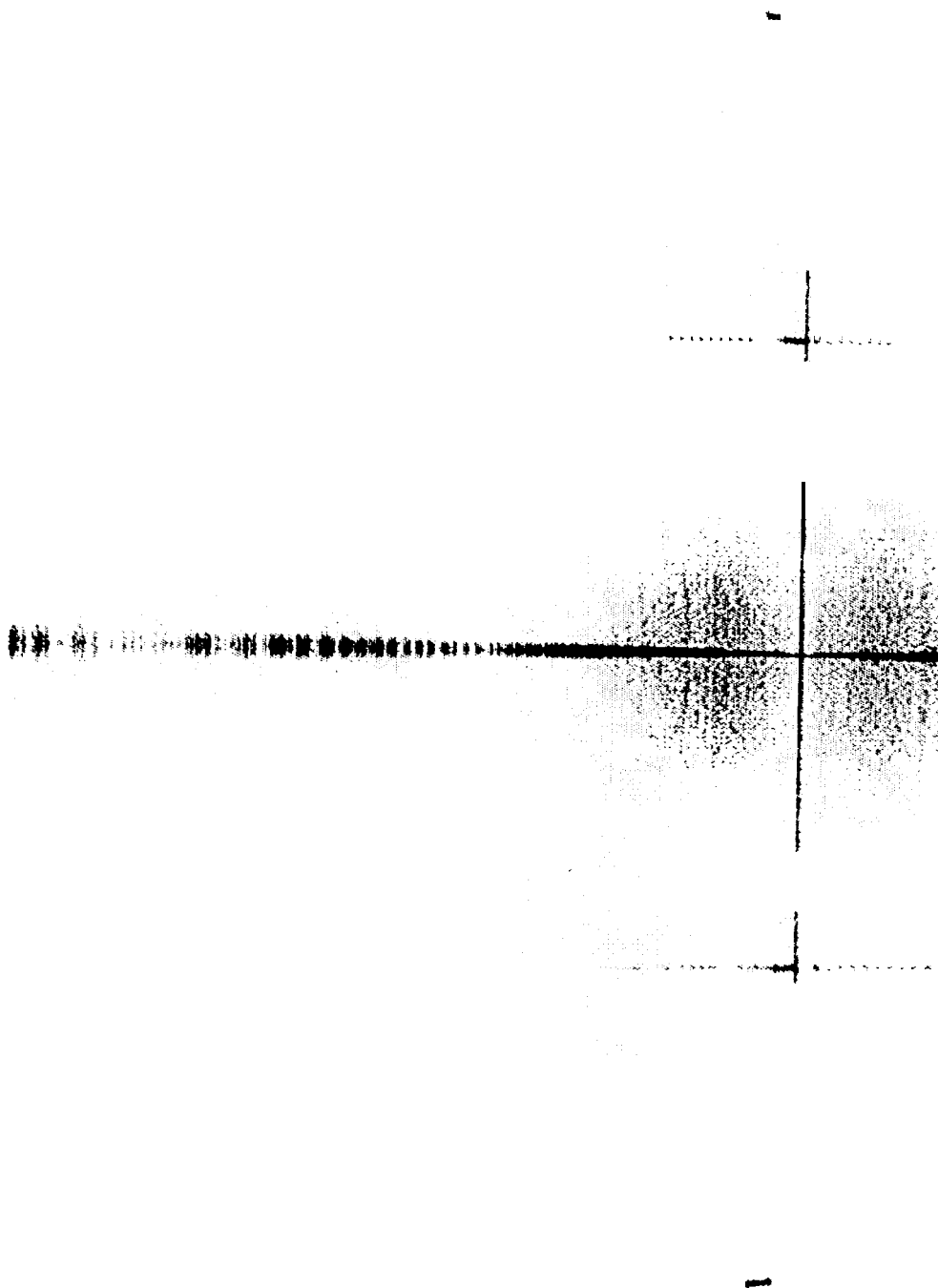
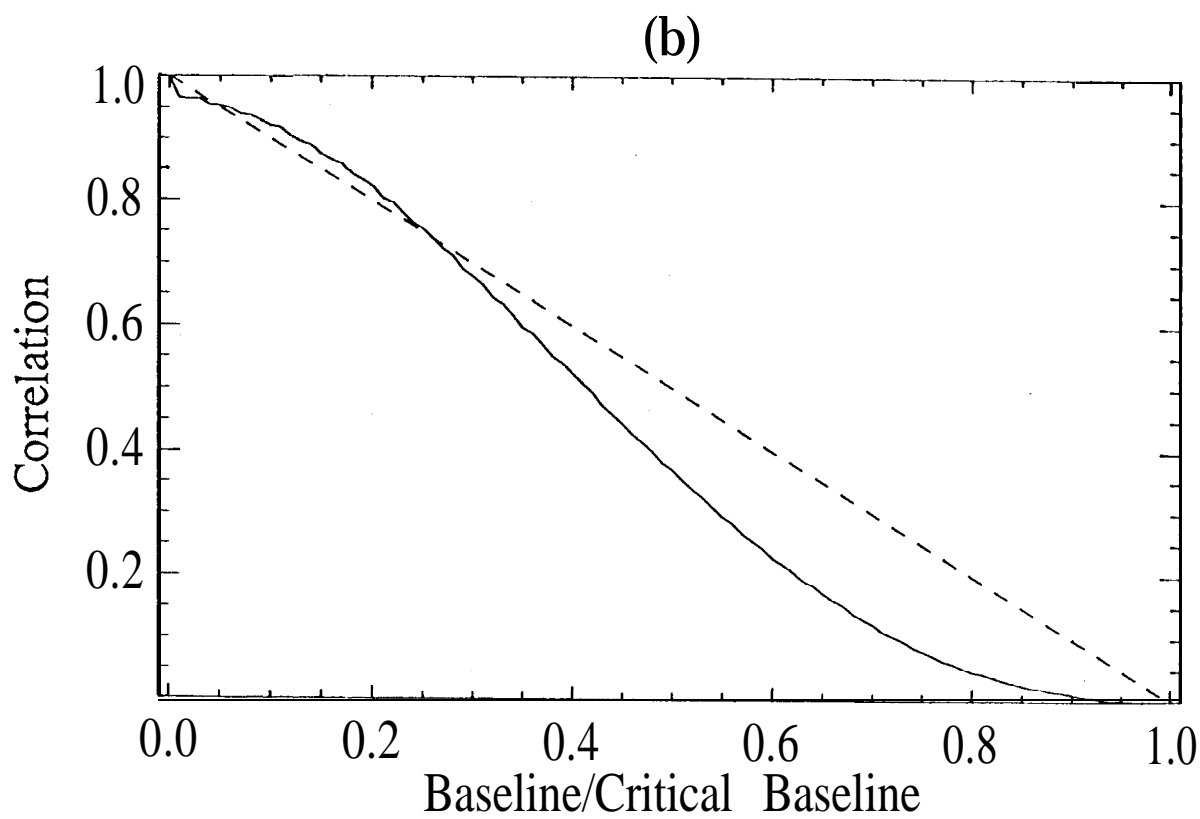
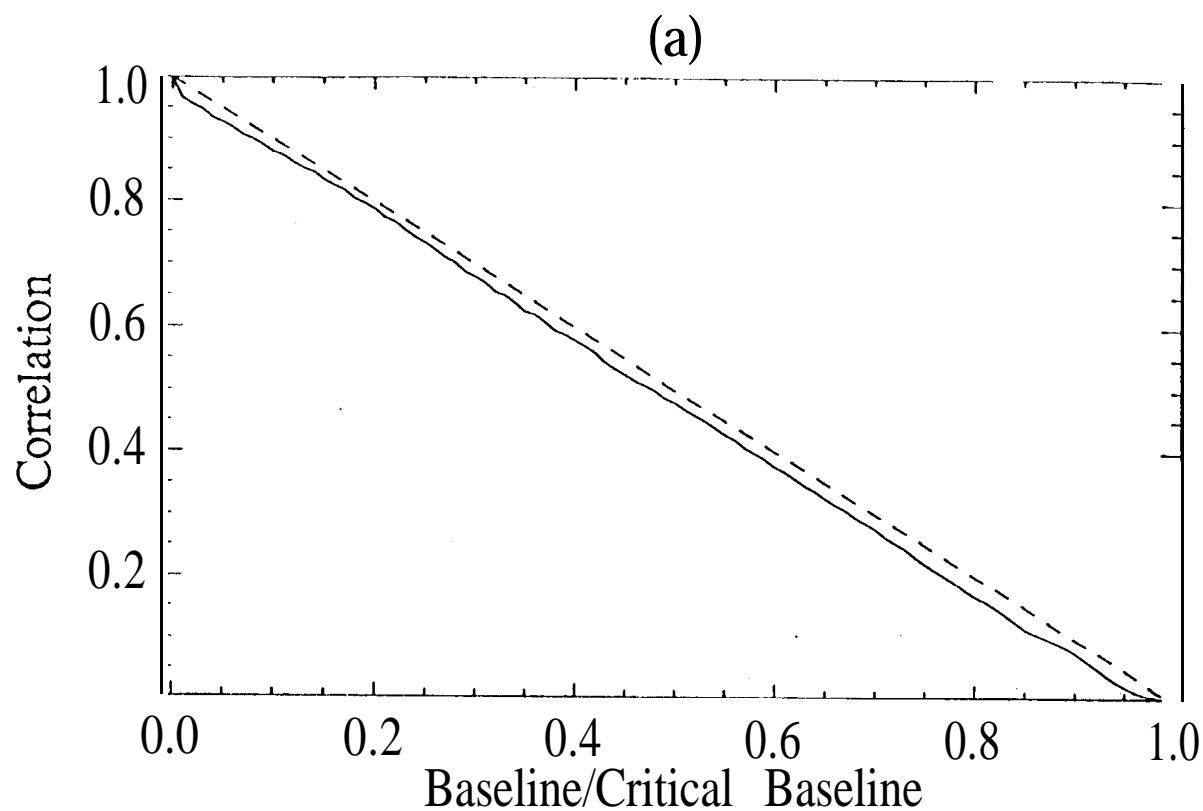


Figure 4



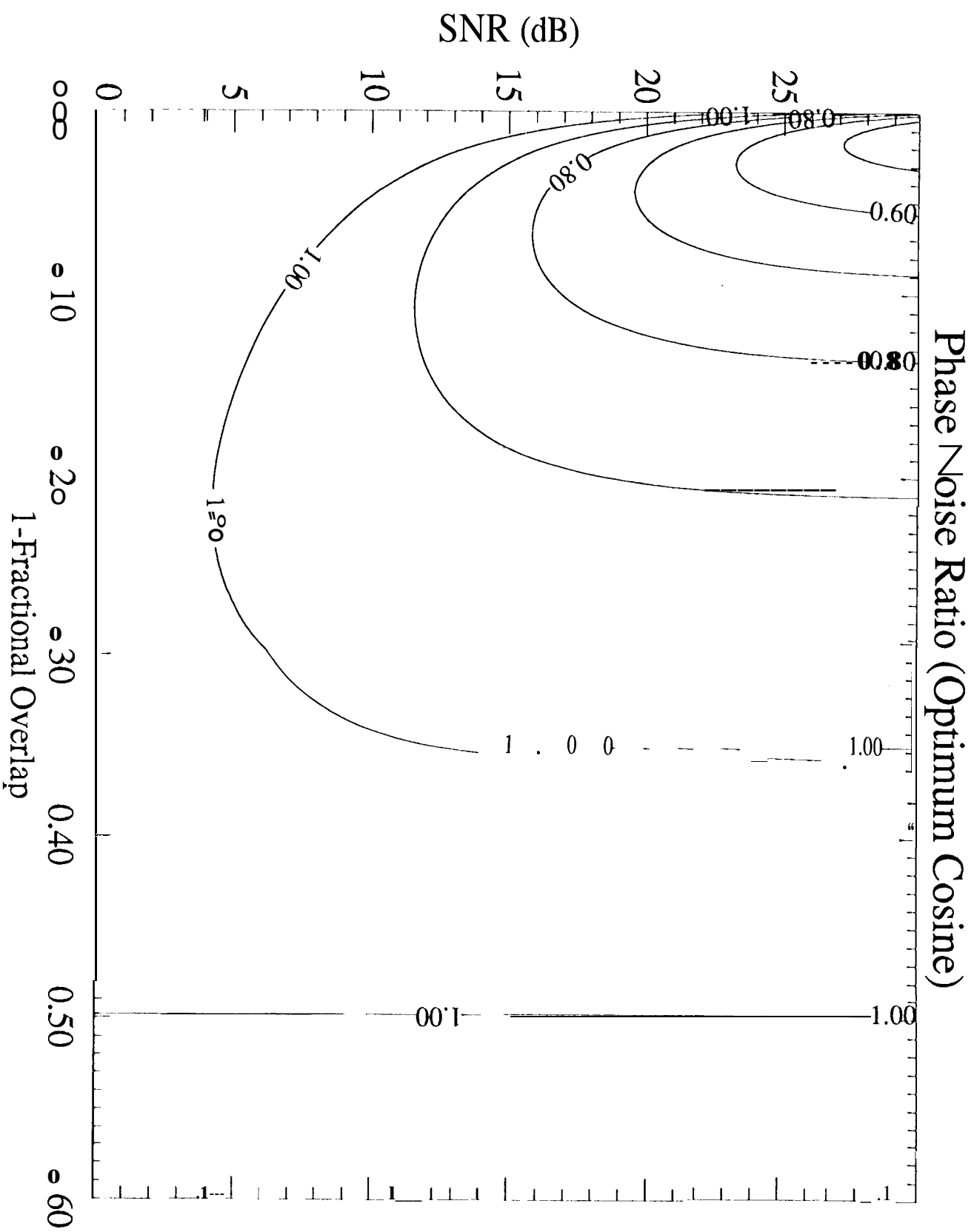


Figure 6a

Phase Noise Ratio (Spectral Truncation)

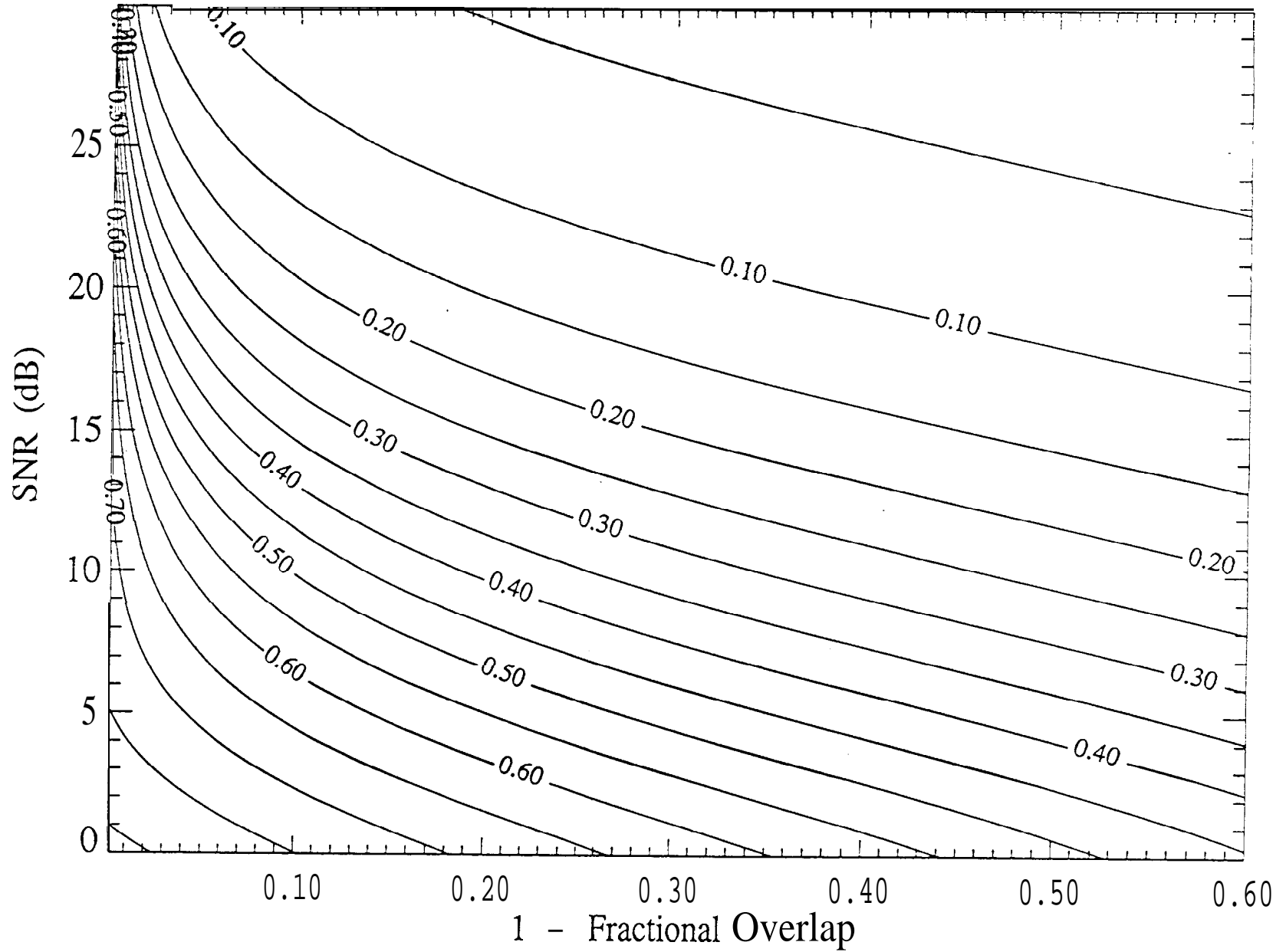


Figure 5b

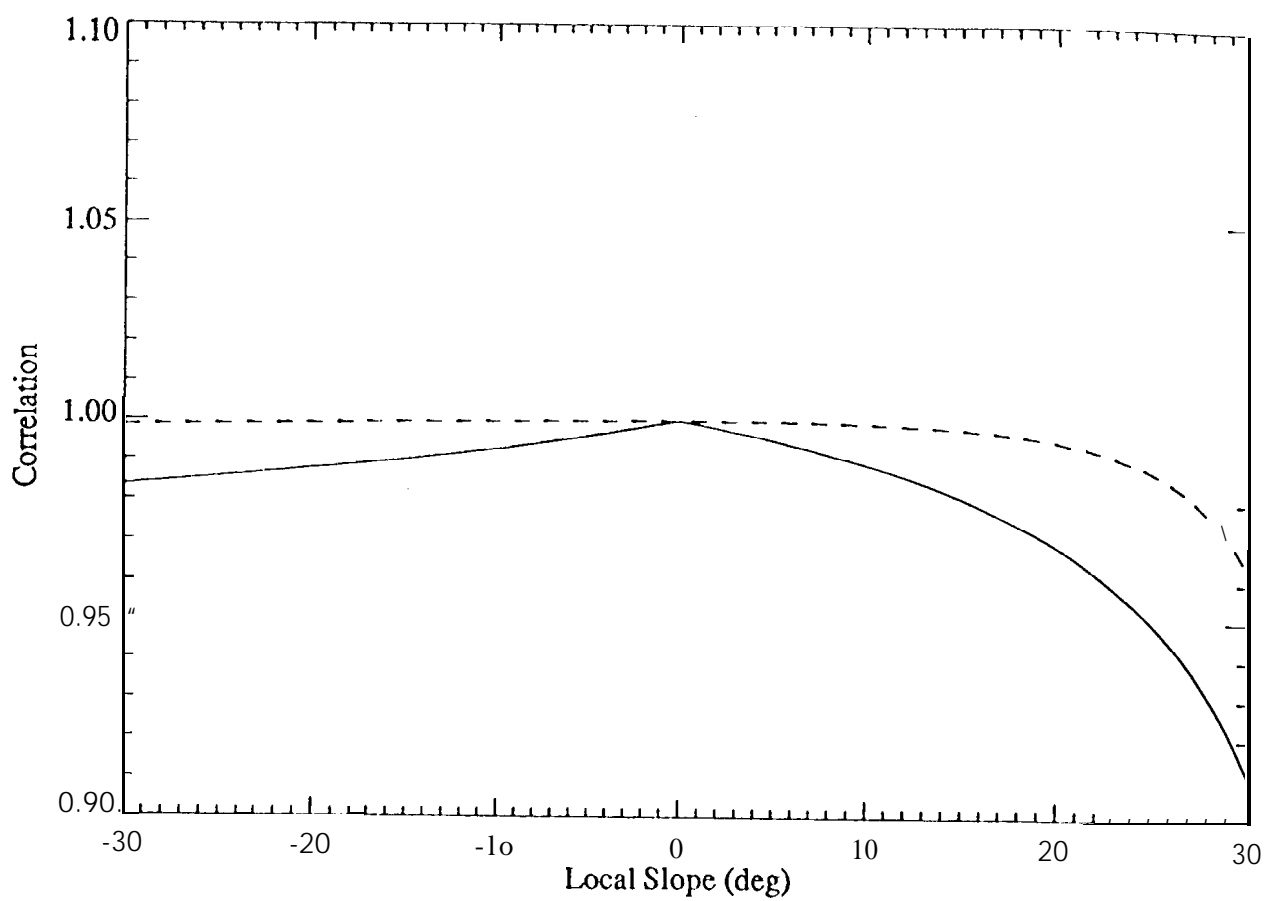
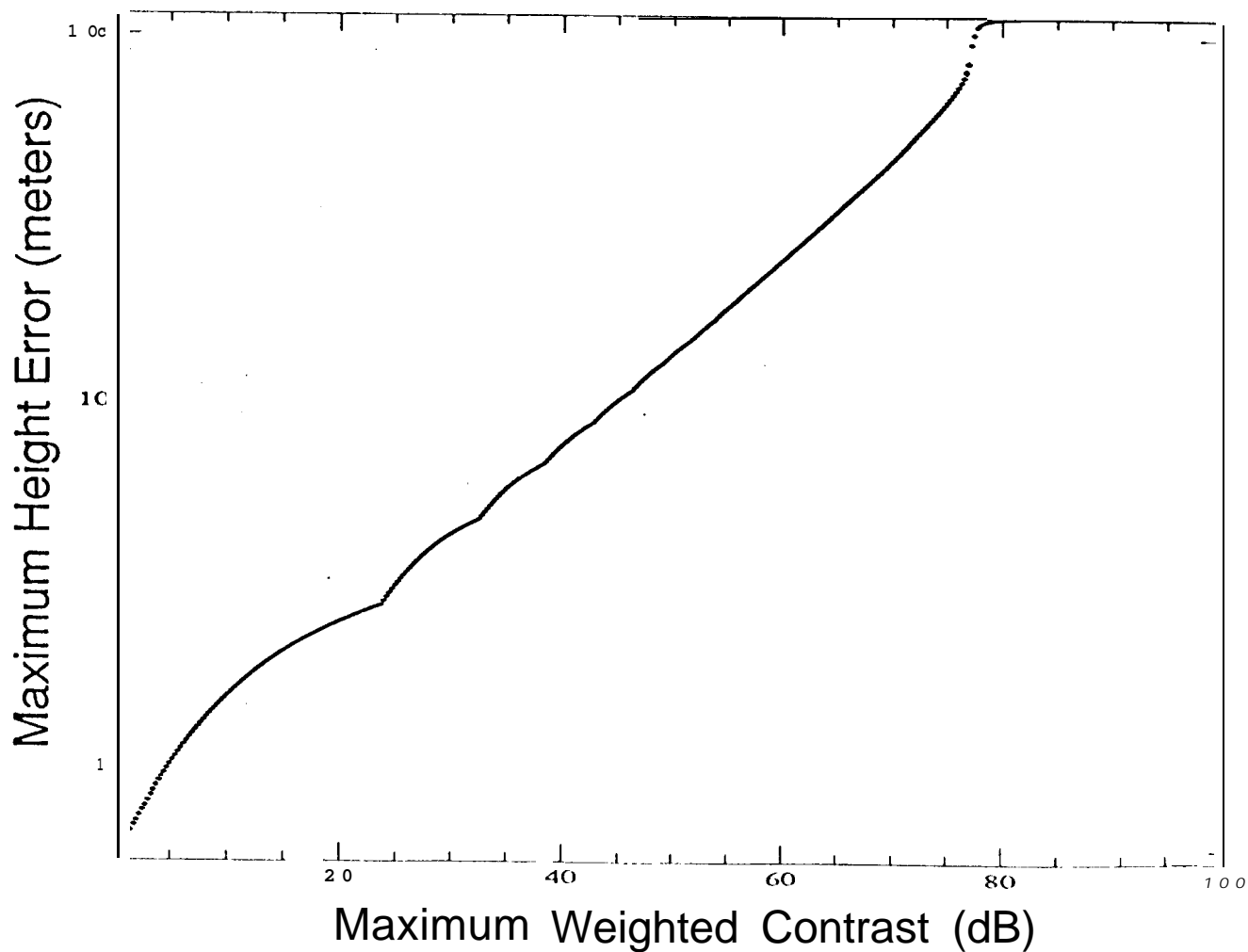
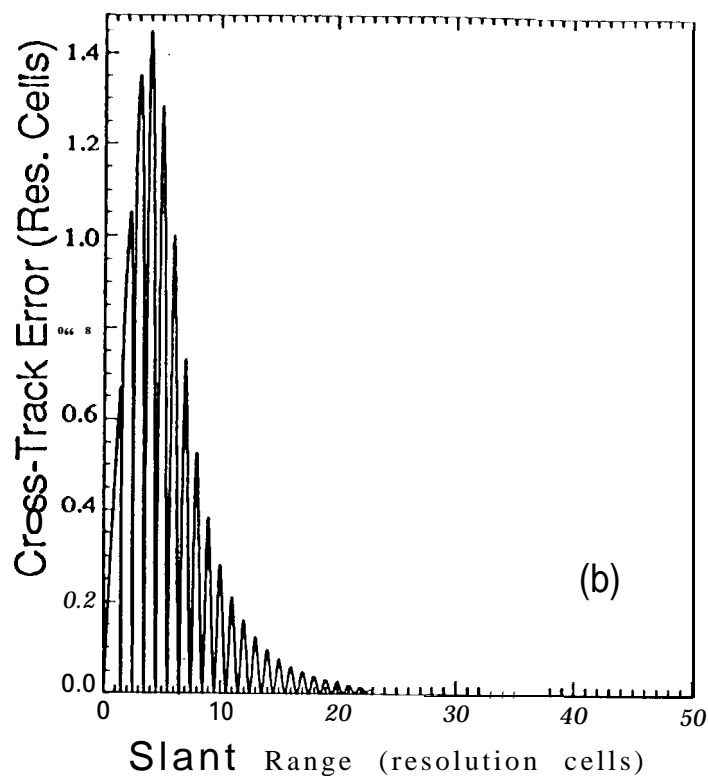
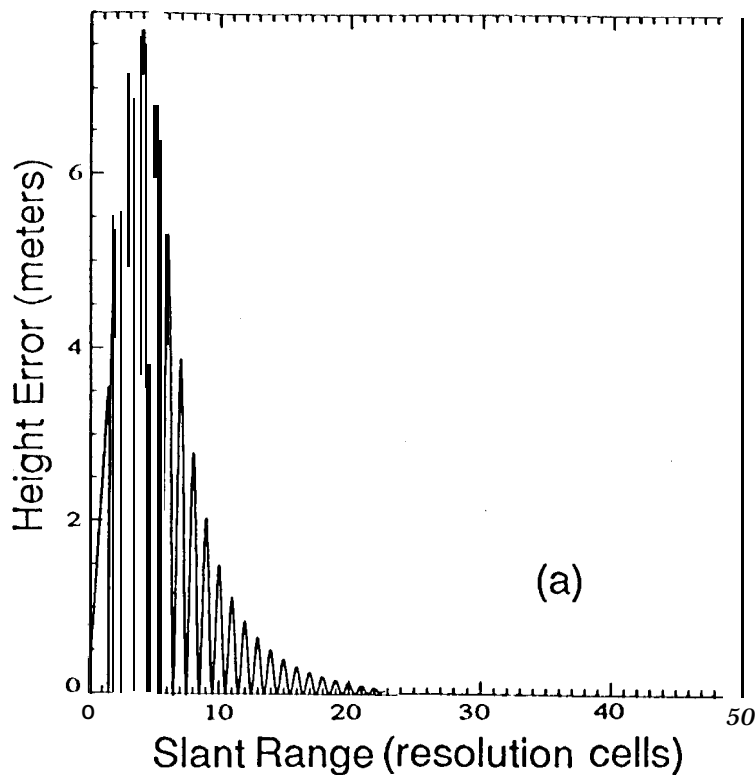
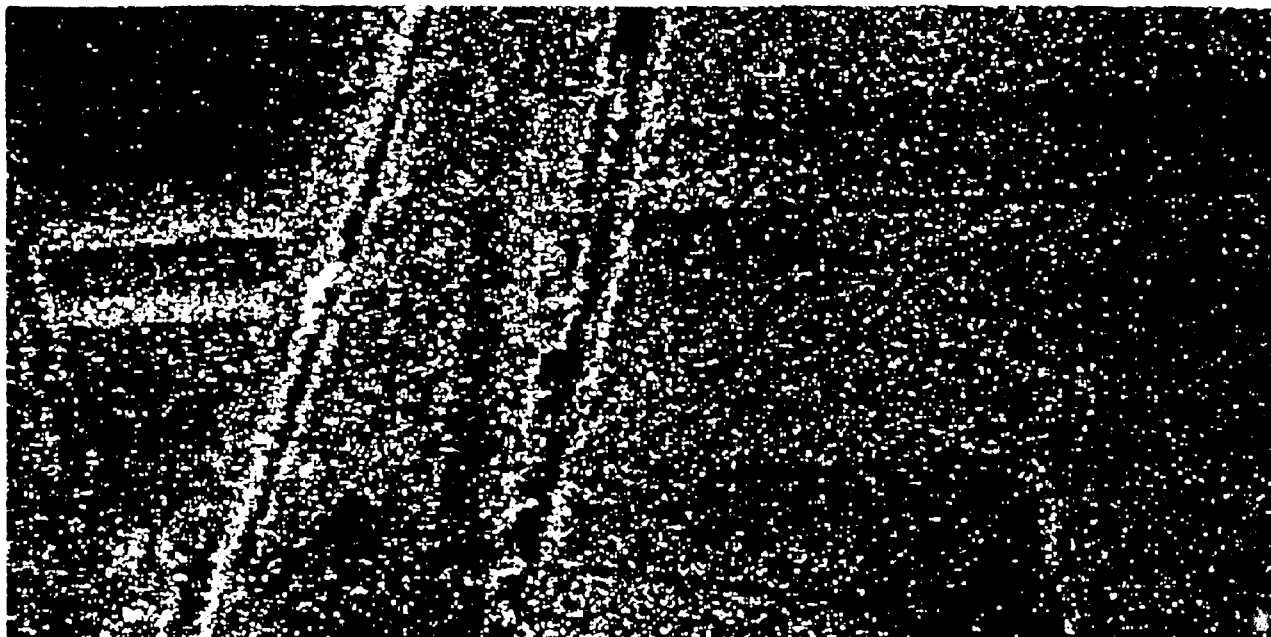


Figure 7





-75

-70

-65

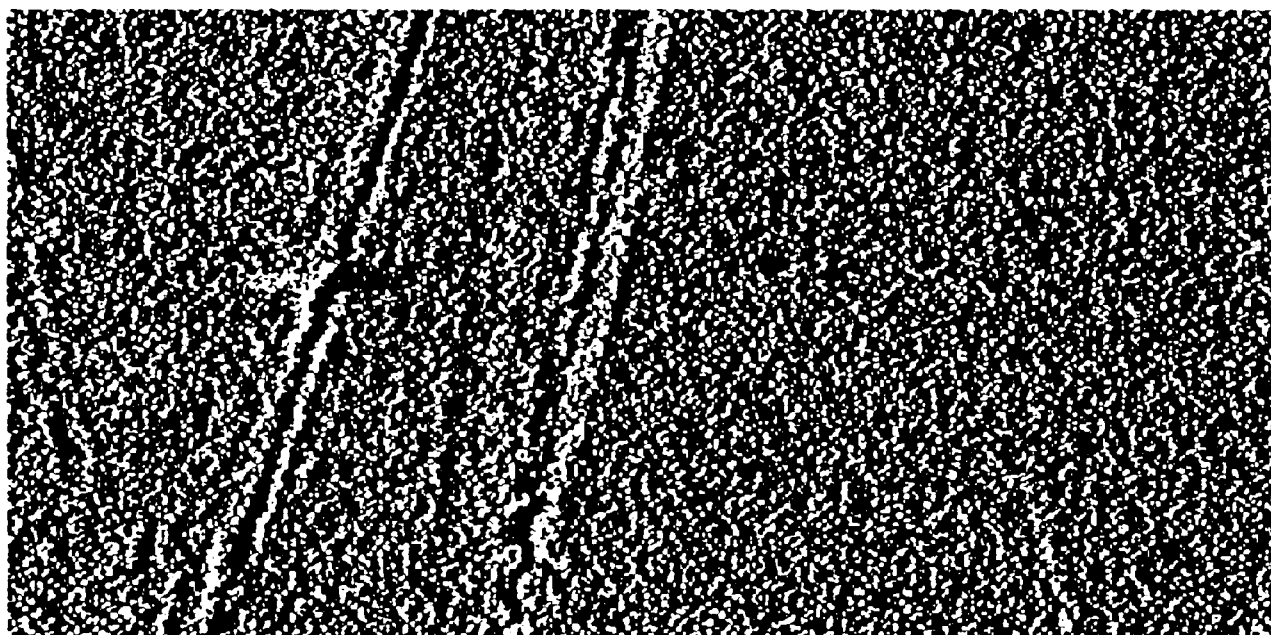
-60

-55

-50

-45

Backscatter (dB)



-5

-3

-1

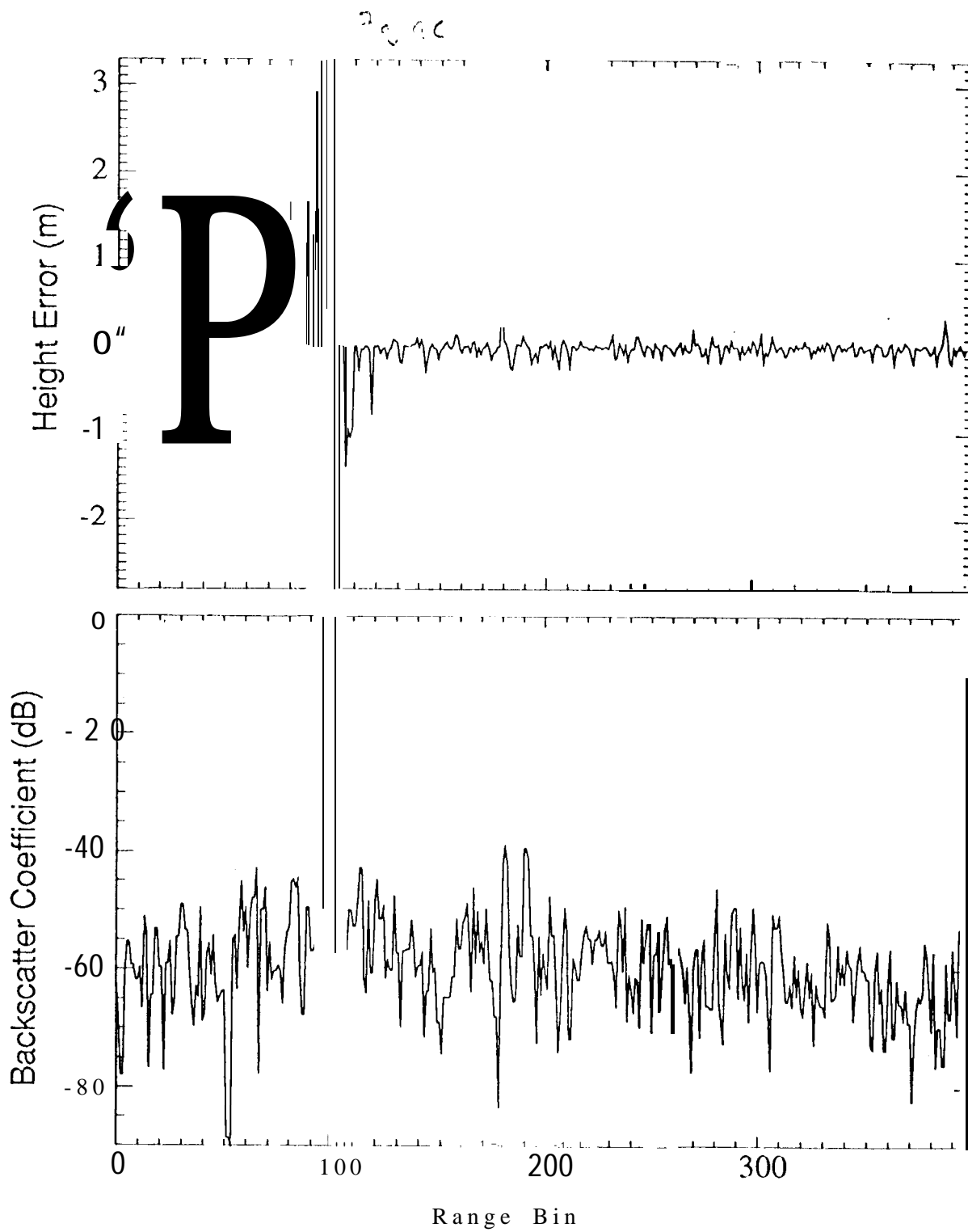
1

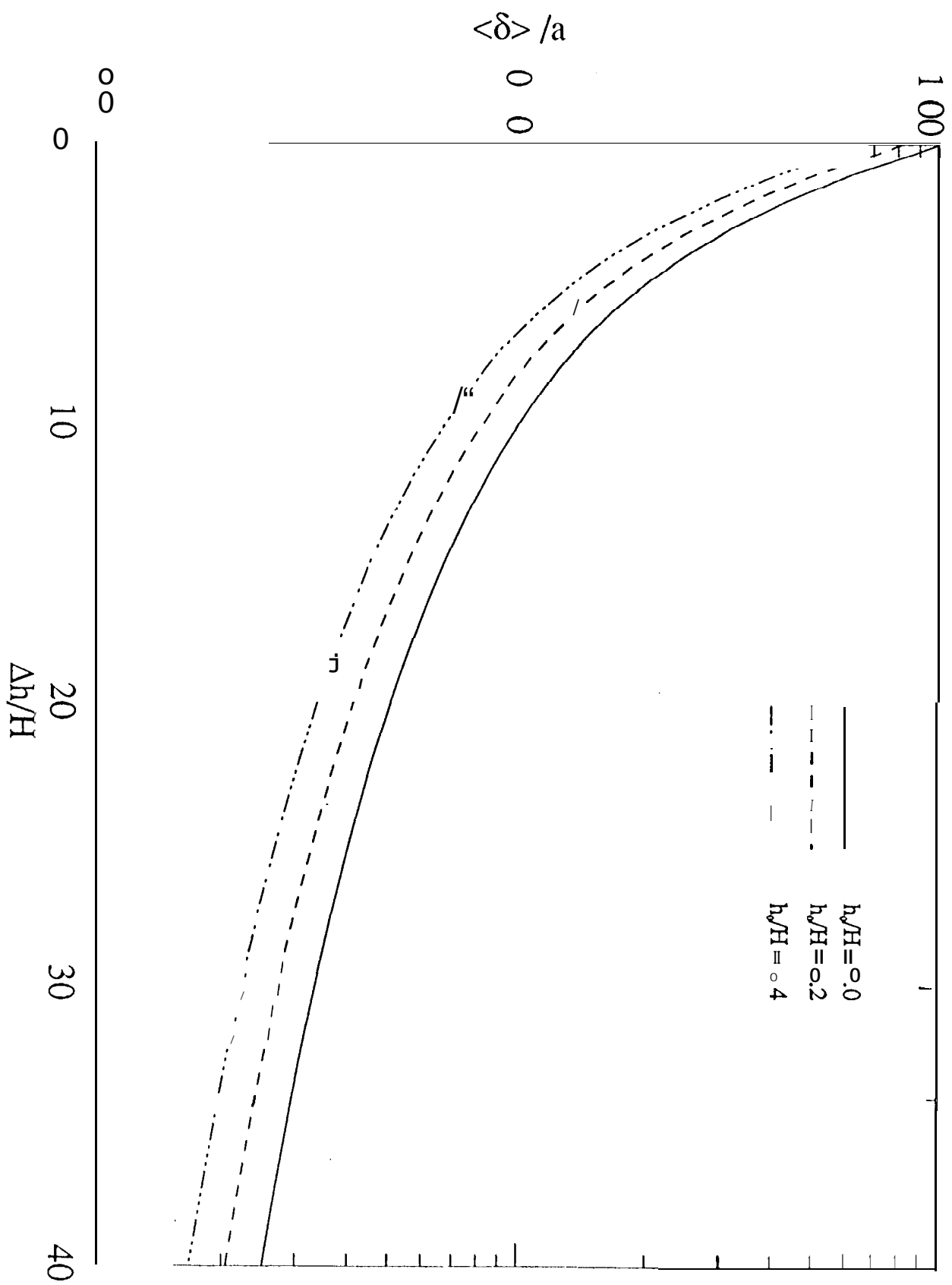
3

5

Height Error (cm)

Fig 9a





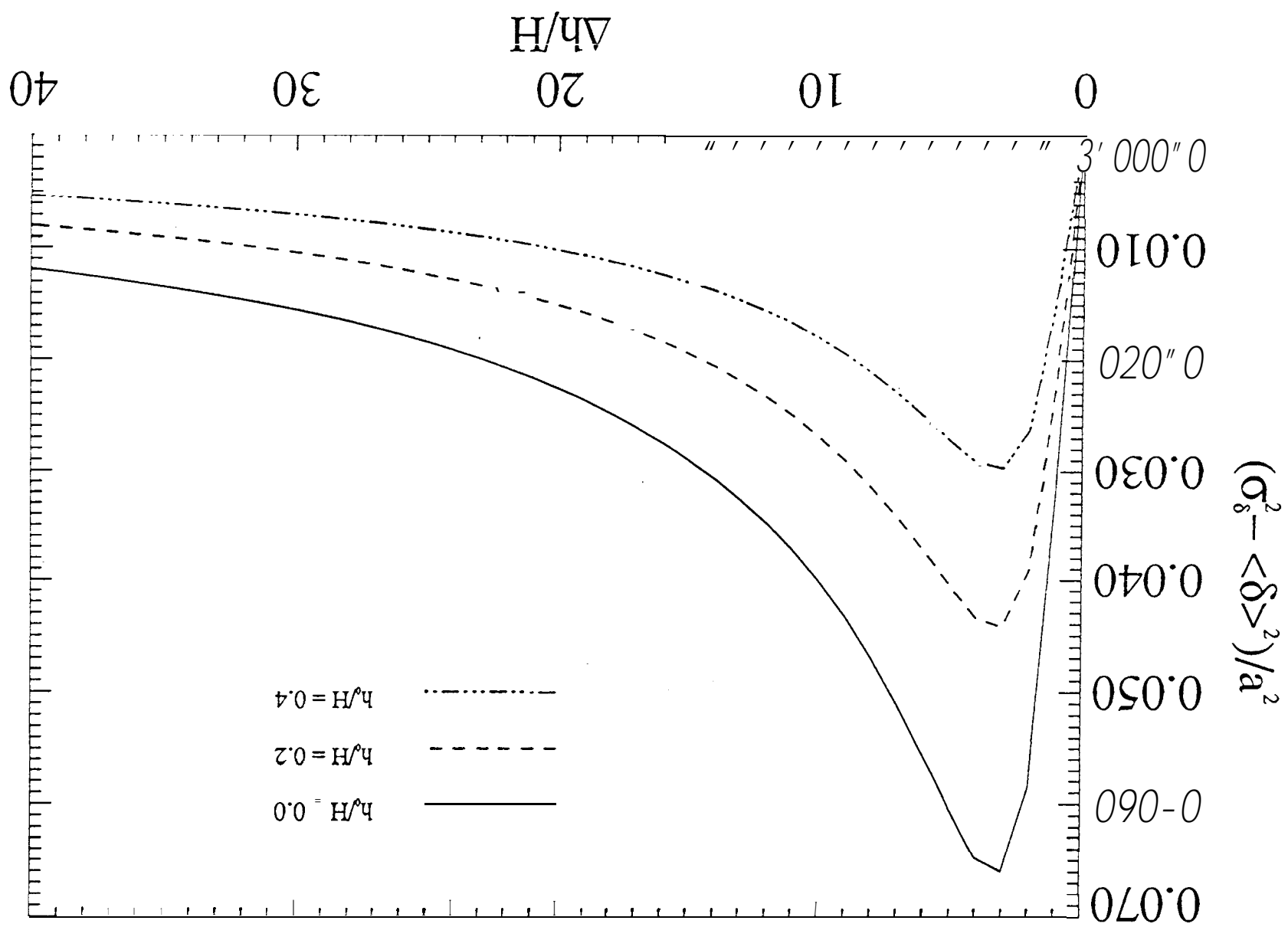


Figure 11

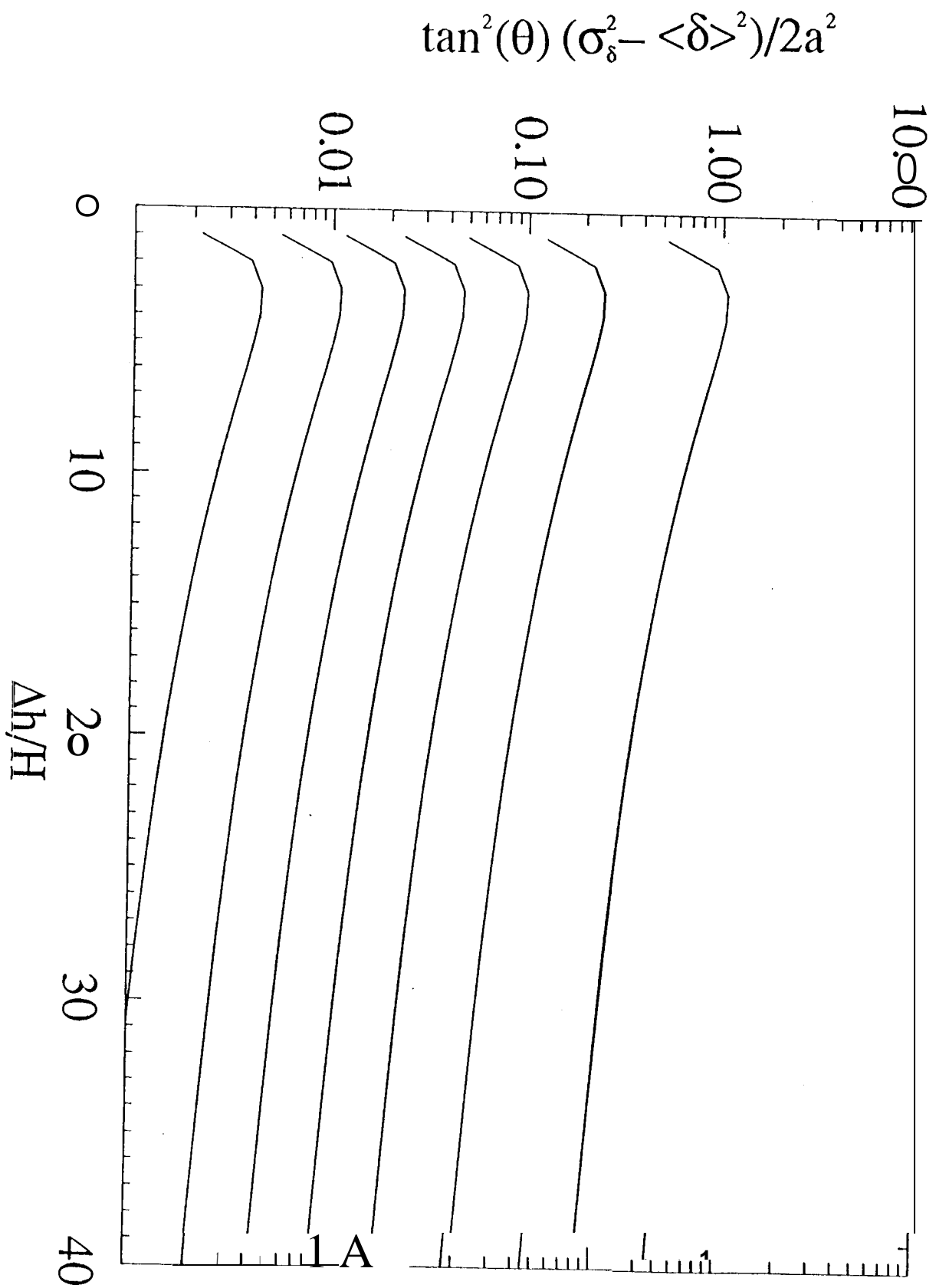


Figure 12

